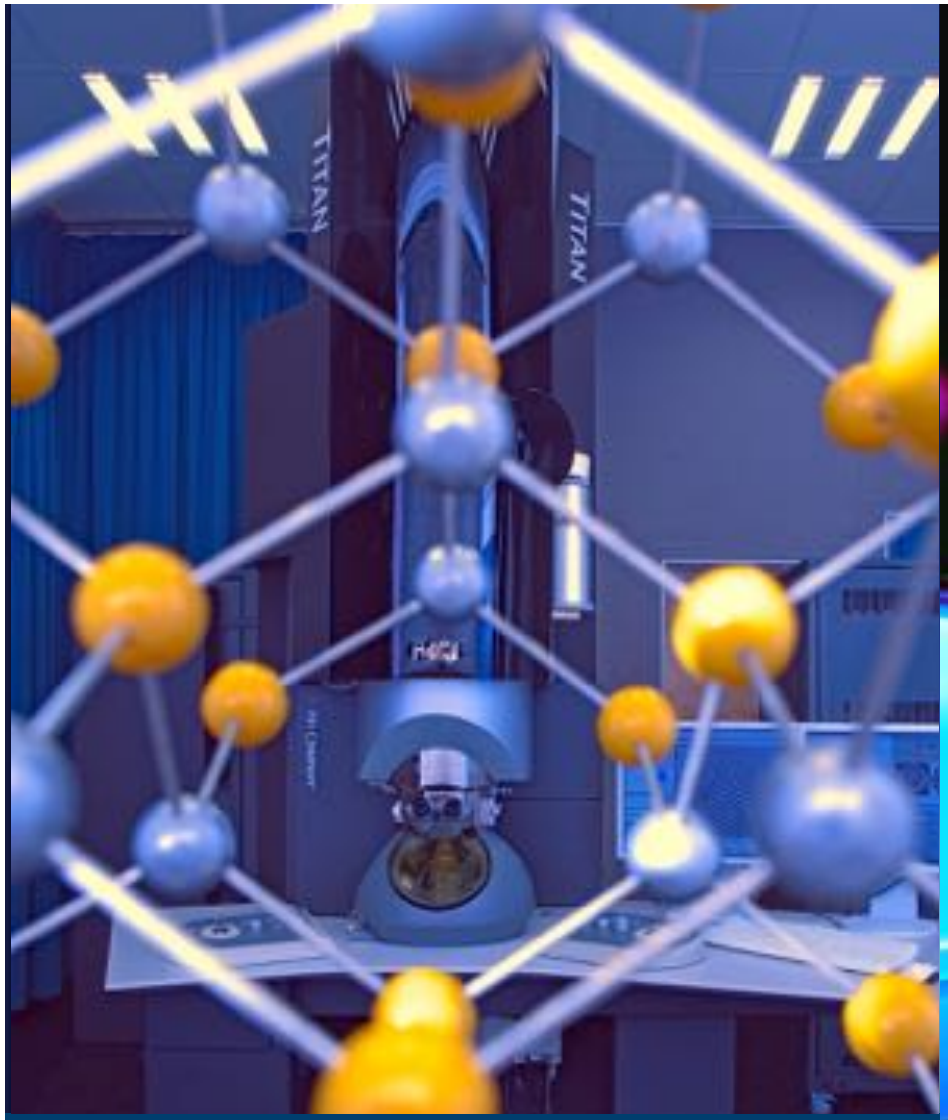

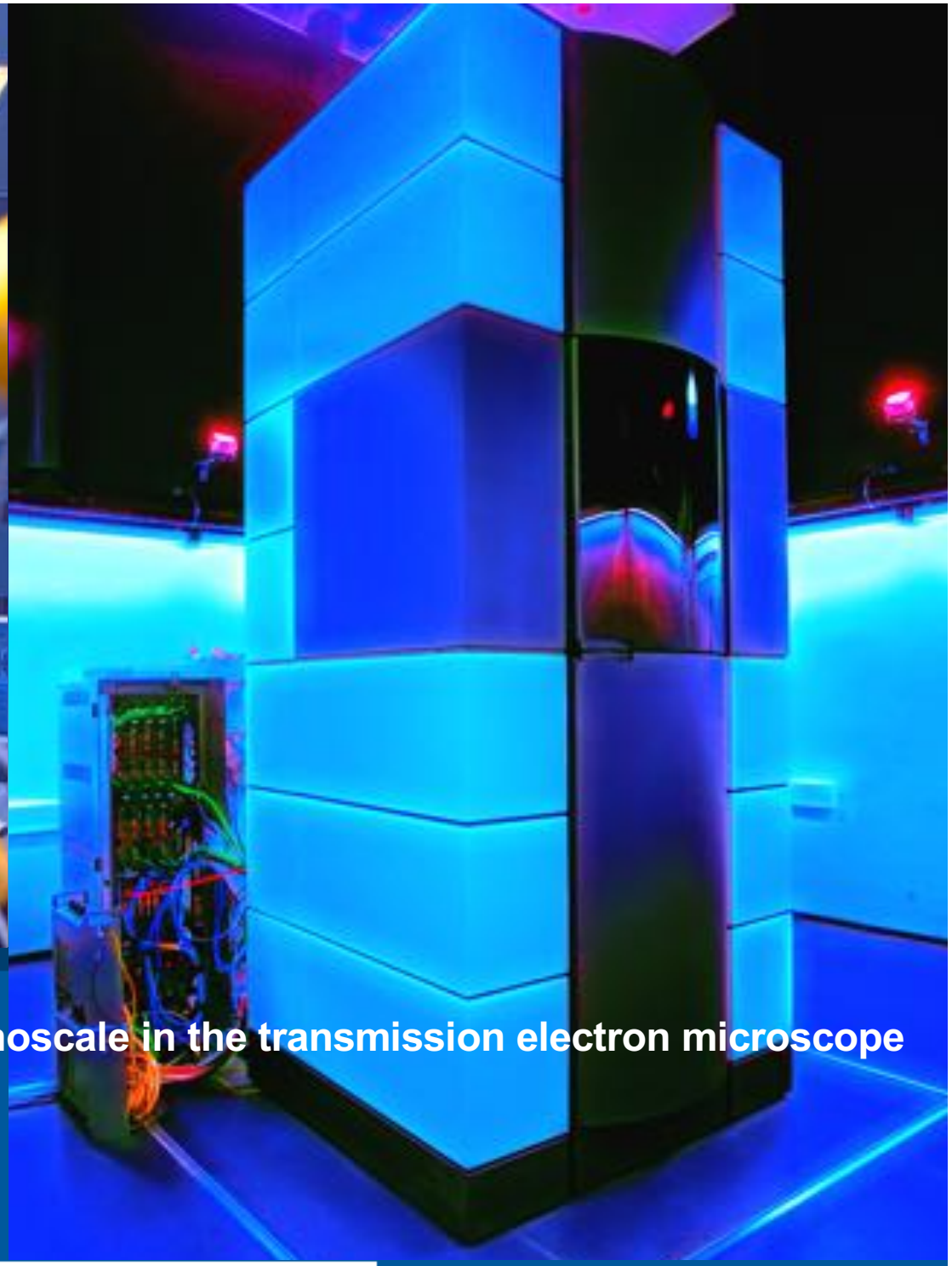

Electromagnetic field mapping at the nanoscale in the transmission electron microscope

Rafal E. Dunin-Borkowski

Forschungszentrum Jülich, Germany

Acknowledgments

Molly McCartney, David Smith, András Kovács, Giulio Pozzi, Zi-An Li, Michael Farle

Fengshan Zheng, Nikolai Kiselev, Stefan Blügel, Kiyou Shibata, Yoshinori Tokura

Jan Caron, Jörn Ungermann, Patrick Diehle, Martin Riese

Trevor Almeida, Adrian Muxworthy, Wyn Williams, Jay Shah, Mihály Pósfai

Attila Kakay, Dirk Grundler, Anna Fontcuberta i Morral

Teresa Wessels, Benjamin Zingsem, Yoshie Murooka

Takeshi Kasama, Marco Beleggia, Matthias Kläui, Laura Heyderman, Mathias Wötzel

Florian Winkler, Sven Borghardt, Beata Kardynal, Matthieu Verstraete

Amir Tavabi, Vadim Migunov, Shery Chang, Christian Dwyer

Lei Jin, Chunlin Jia, Knut Urban, Juri Barthel, Andreas Thust, Joachim Mayer

Lothar Houben, Maya Bar Sadan, Niels de Jonge, Chris Boothroyd, Jörg Jinschek

David Cooper, Philippa Somodi, Alison Twitchett-Harrison, Paul Midgley

Miriam Varon, Victor Puntes, Cathrine Frandsen

Richard Harrison, Josh Feinberg, Andrew Putnis, Alexander Wei, Steve Tripp

Outline

- Introduction to TEM of magnetic fields and electrostatic potentials
- Overview of Lorentz TEM techniques
- Basics of off-axis electron holography
- Instrumental requirements
- Experimental design

Basics

- Medium resolution electron holography of magnetic fields
- Medium resolution electron holography of electrostatic potentials
- High-resolution electron holography
- Dynamical effects
- Electron holography of working devices
- Other modes of electron holography
- Future prospects and challenges

State of the art

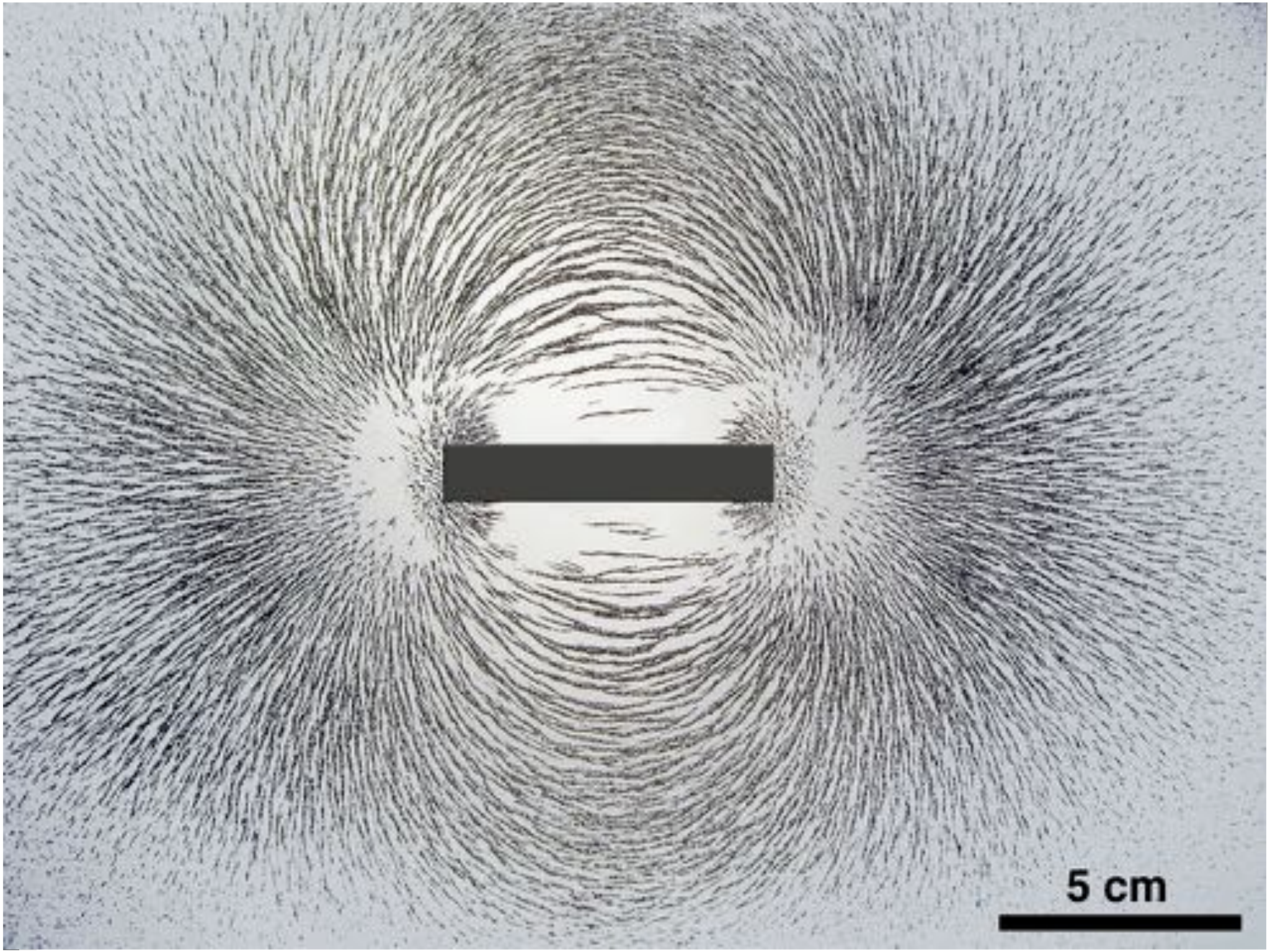
5 cm

Multi-walled carbon nanotube containing Fe

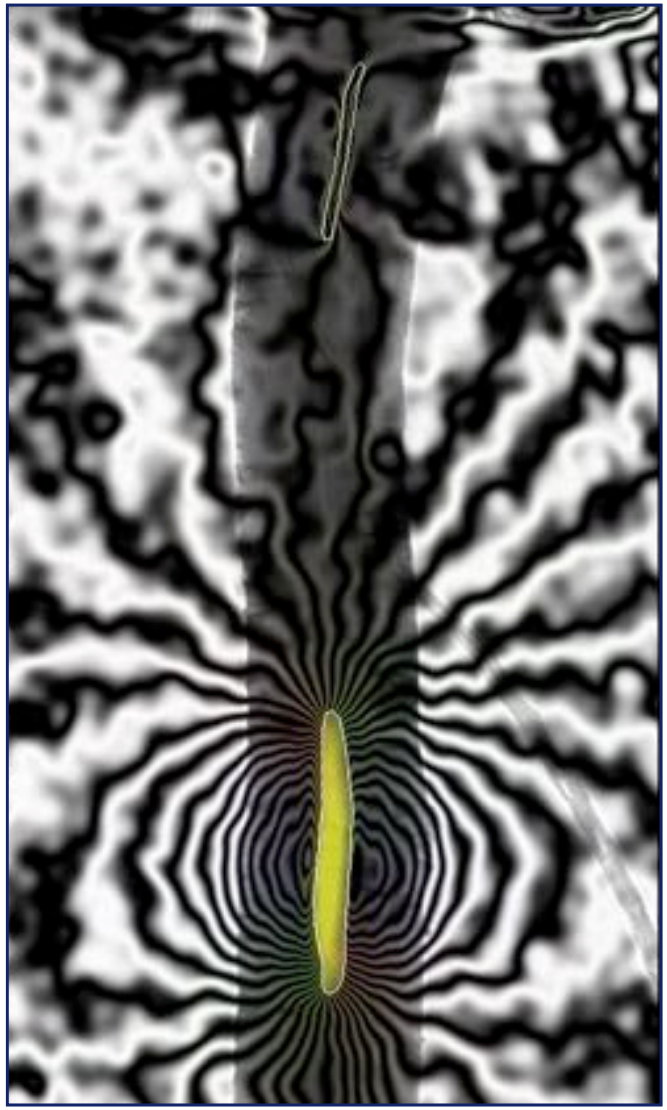

K. Koziol, A.H. Windle

High-resolution TEM

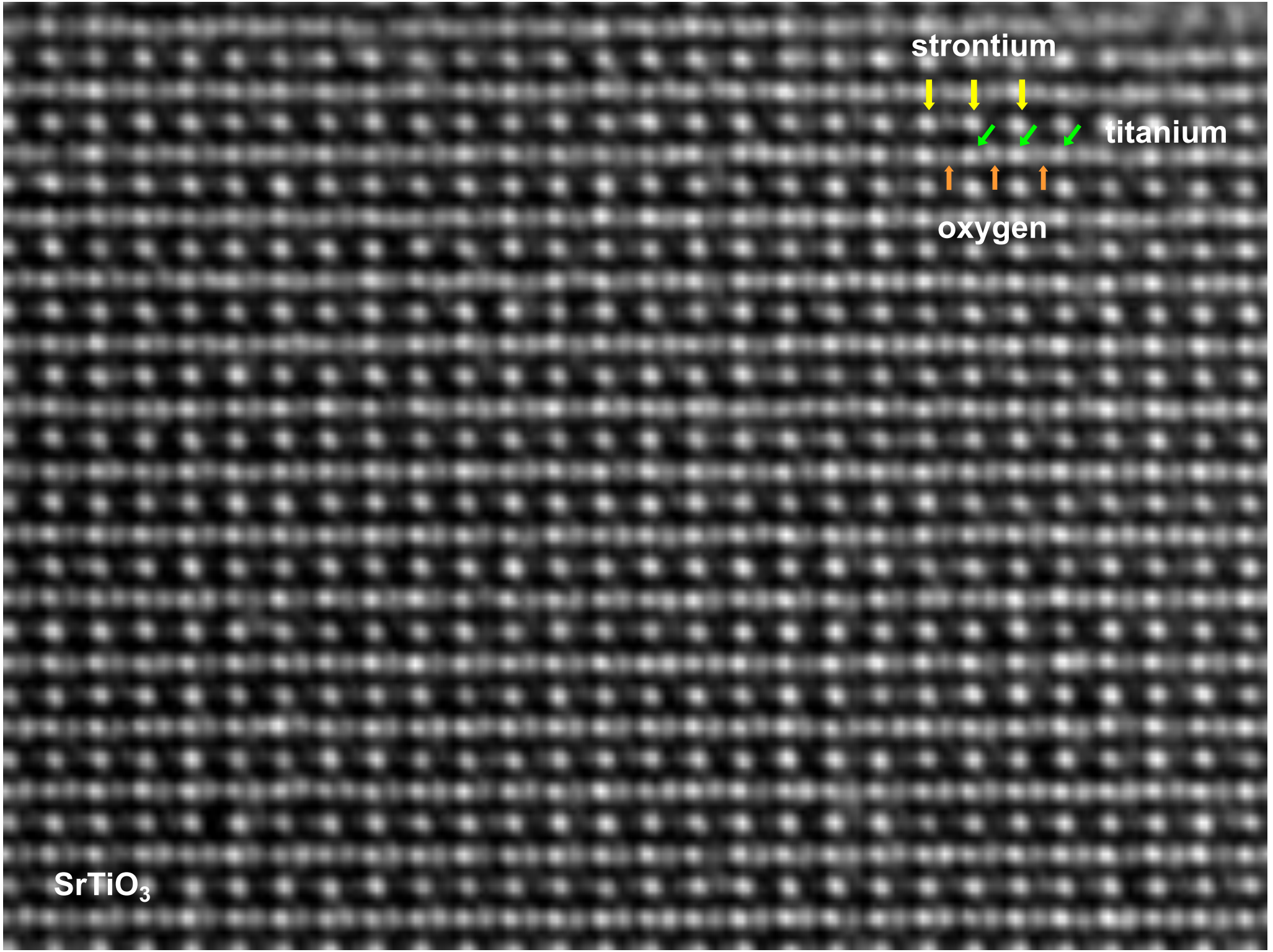
strontium
titanium
oxygen
$SrTiO_3$

High-resolution TEM

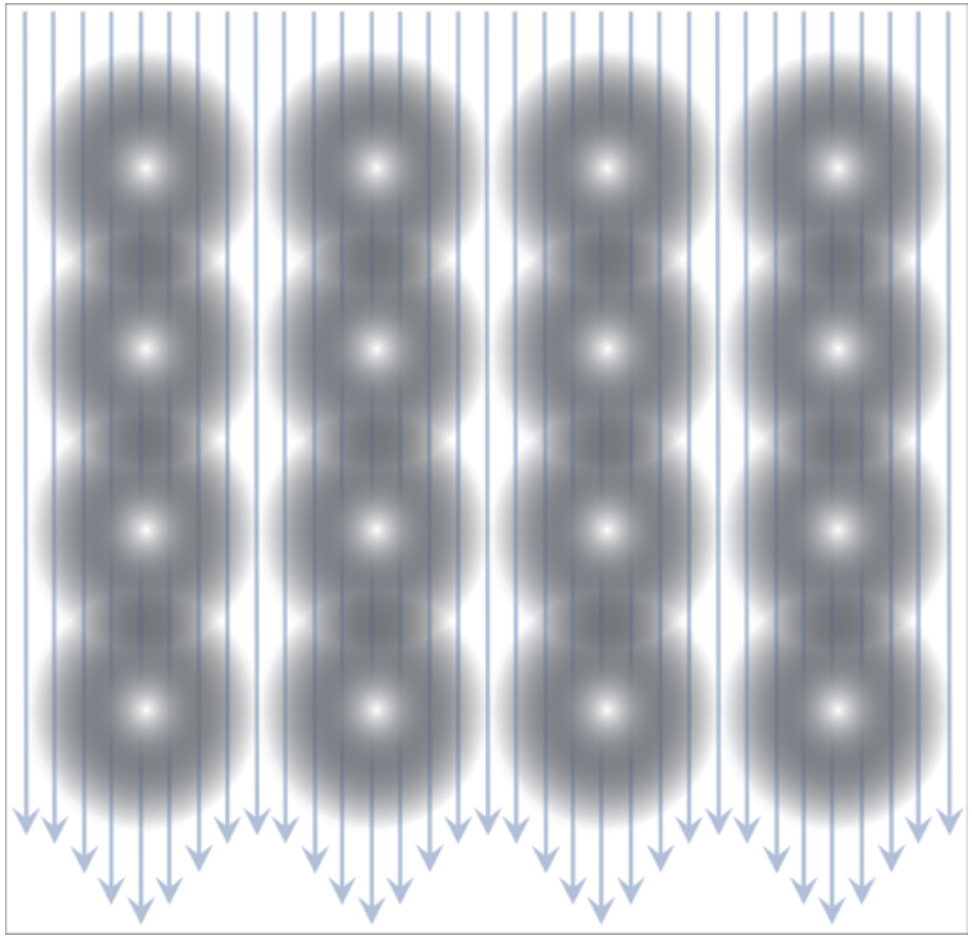

Locally varying phase shift

Measurement of electron optical phase

Phase contrast techniques in the (S)TEM

- In-line electron holography
- STEM differential phase contrast (or central beam deflection)
- Ptychography
- Diffractive imaging
- Off-axis electron holography

Definition and importance of the phase

Basis of off-axis electron holography

Phase shift:

$$\phi(x,y) = C_E \int_{z=-\infty}^{z=+\infty} V(x,y,z)dz - \left(\frac{e}{\hbar}\right) \int_{z=-\infty}^{z=+\infty} \int_{x=-\infty}^{x=x} B_x(x,y,z)dzdx$$

Sensitive to:

magnetic fields

composition

density

bonding/ ionicity

electrostatic fields at depletion layers

electrostatic fringing fields outside materials

Off-axis electron holography

If V(x) and B(x) do not vary in the incident electron beam direction, then:

Phase shift:

$$\phi(x) = C_E V(x) t(x) - \left(\frac{e}{\hbar}\right) \int B_{\perp}(x) t(x)\, dx$$

Sensitive to: **magnetic fields**

composition

density

bonding/ ionicity

electrostatic fields at depletion layers

electrostatic fringing fields outside materials

Lorentz imaging of magnetic thin films

Lorentz transmission electron microscopy

Fresnel mode of Lorentz microscopy

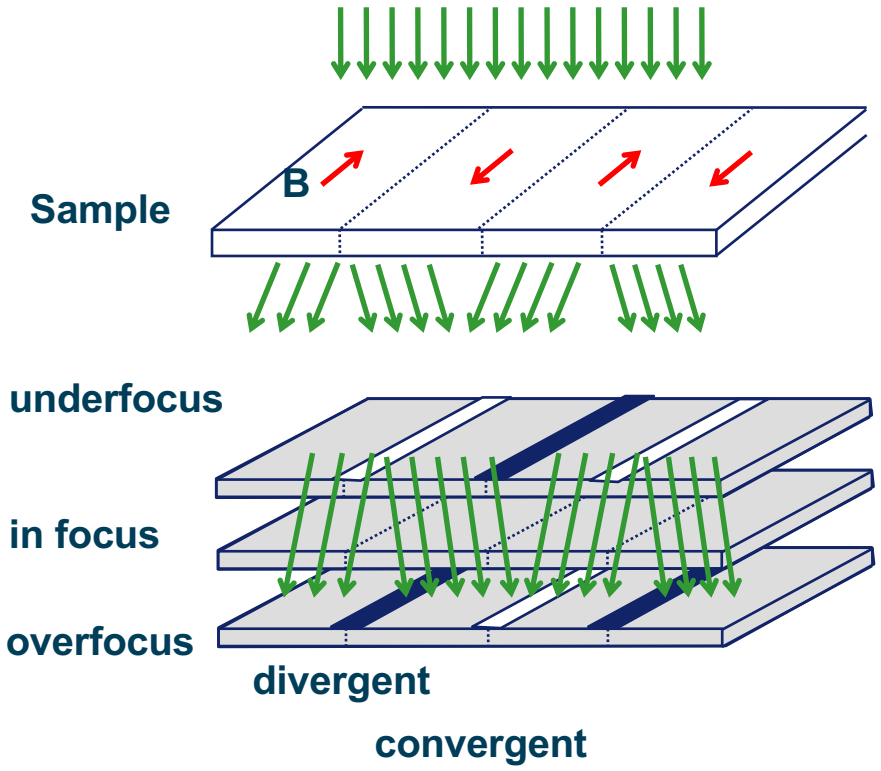

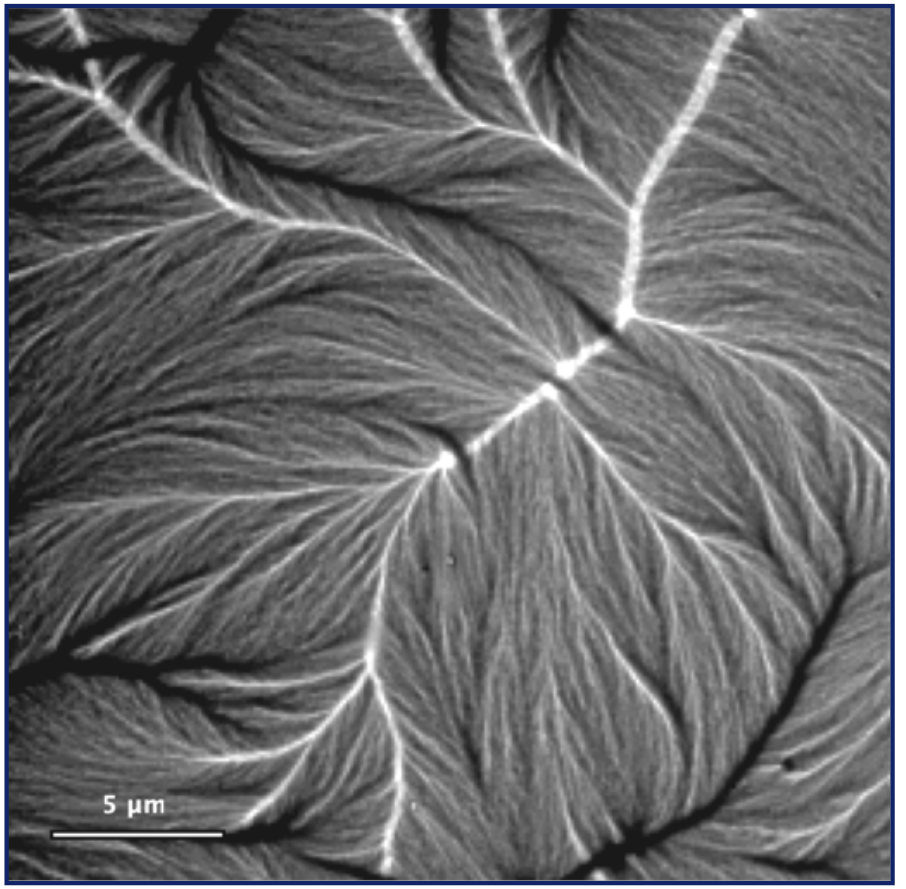

Electron holography

Historical background

1947 Denis Gabor proposes holography ("whole writing") as a means to correct for electron microscope aberrations - **Nobel prize 1971.**

1936 First commercial TEM - Metropolitan Vickers EM1.

1932 E. Ruska and M. Knoll proposed the idea of an electron microscope - **Nobel prize 1986.**

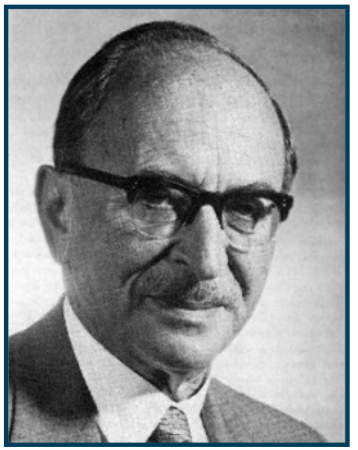

Denis Gabor

Electron microscope built by Ruska and Knoll in Berlin in the 1930s.

1927 G.P. Thomson and A. Reid with C.J. Davisson and L.H. Germer showed the electron was a wave - first electron diffraction experiments - **Nobel prize 1937.**

1897 J.J. Thomson discovers the electron (particle with a certain charge-to-mass ratio) - **Nobel prize 1906.**

Off-axis electron holography

Gottfried Möllenstedt
(1913-1997)
Tübingen, Germany

Invention of electron biprism in 1954

TEM mode of off-axis electron holography

Off-axis electron holography

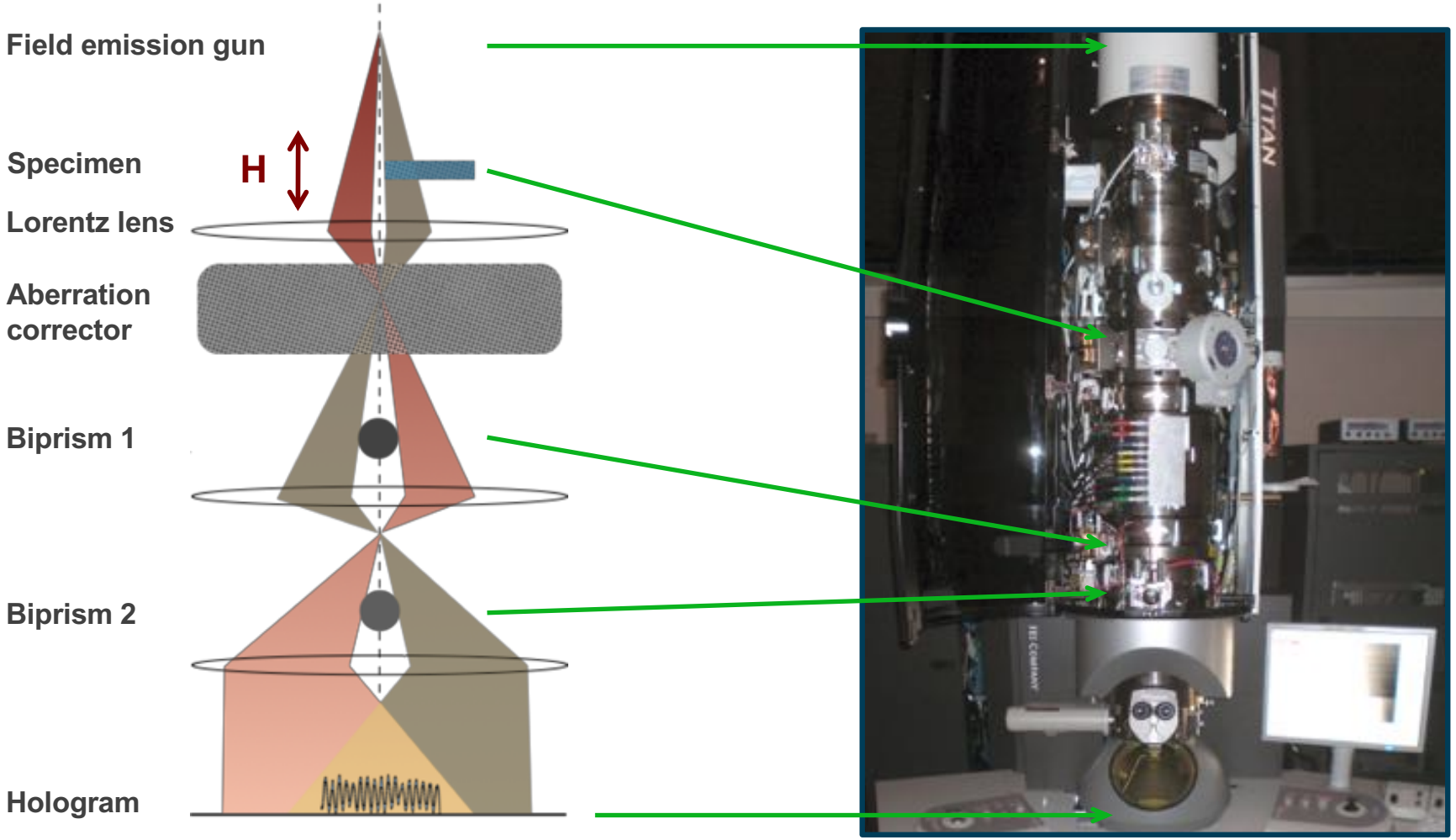

Electron holography provides access to the phase shift of the electron wave that passes through a specimen in the TEM. The phase shift can be related to the in-plane magnetic induction and to the electrostatic potential within and around the specimen, projected in the electron beam direction.

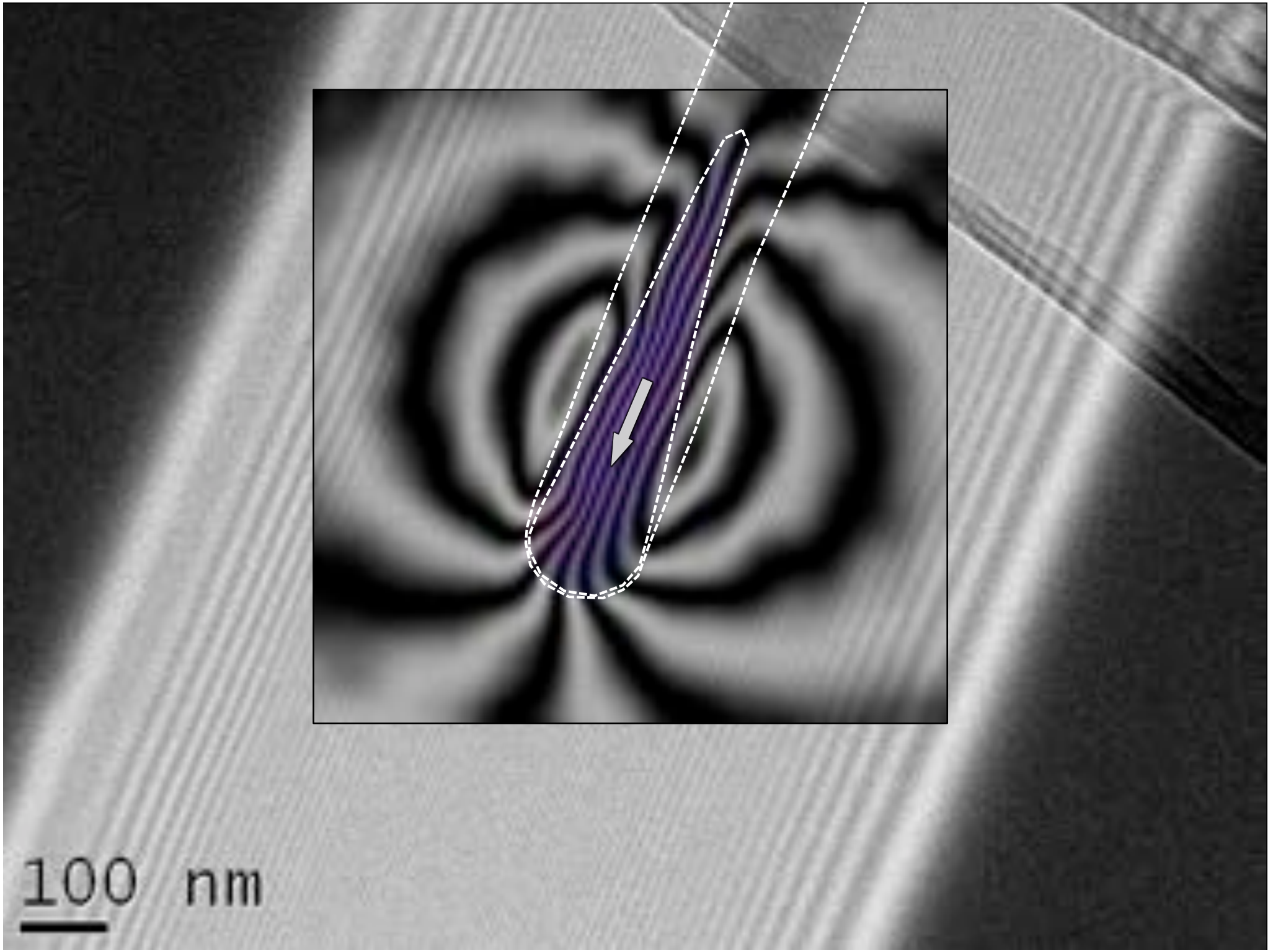
100 nm

Basis of off-axis electron holography

Schematic illustration of set-up for generating off-axis electron holograms.

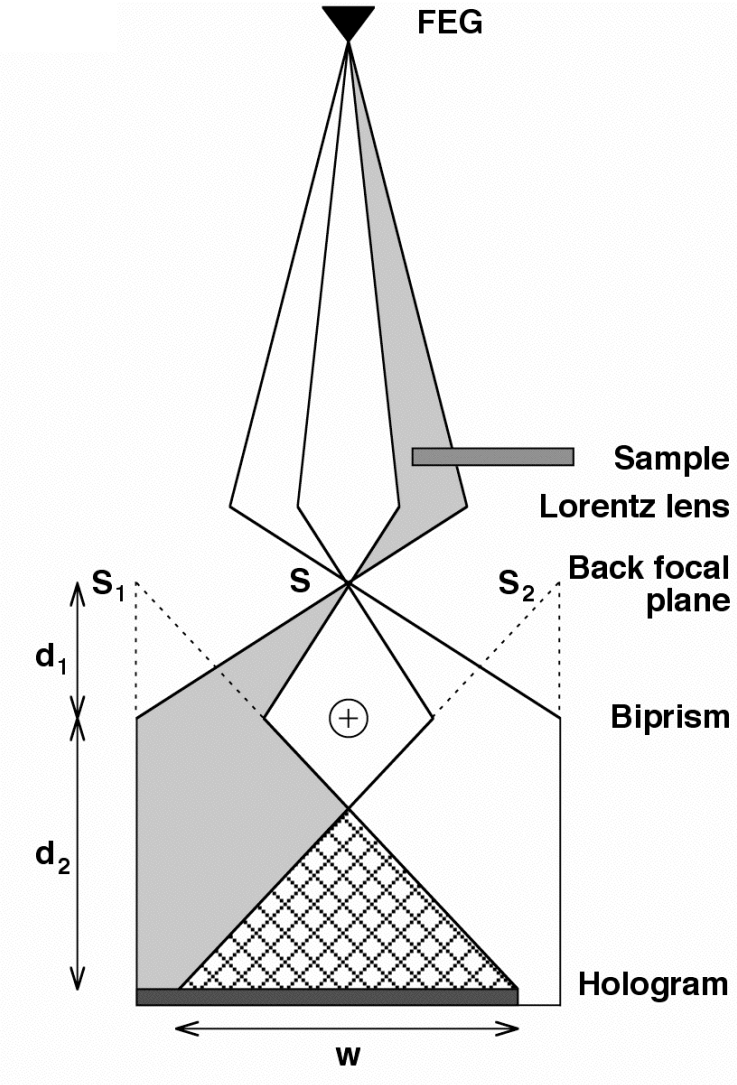

- The sample occupies approximately half the field of view.
- The field-emission electron gun (FEG) electron source provides coherent illumination.
- The electrostatic biprism causes overlap of the object and (vacuum) reference waves.
- The Lorentz lens allows imaging of magnetic materials in field-free conditions.

Basis of off-axis electron holography

Schematic illustration of set-up for generating off-axis electron holograms.

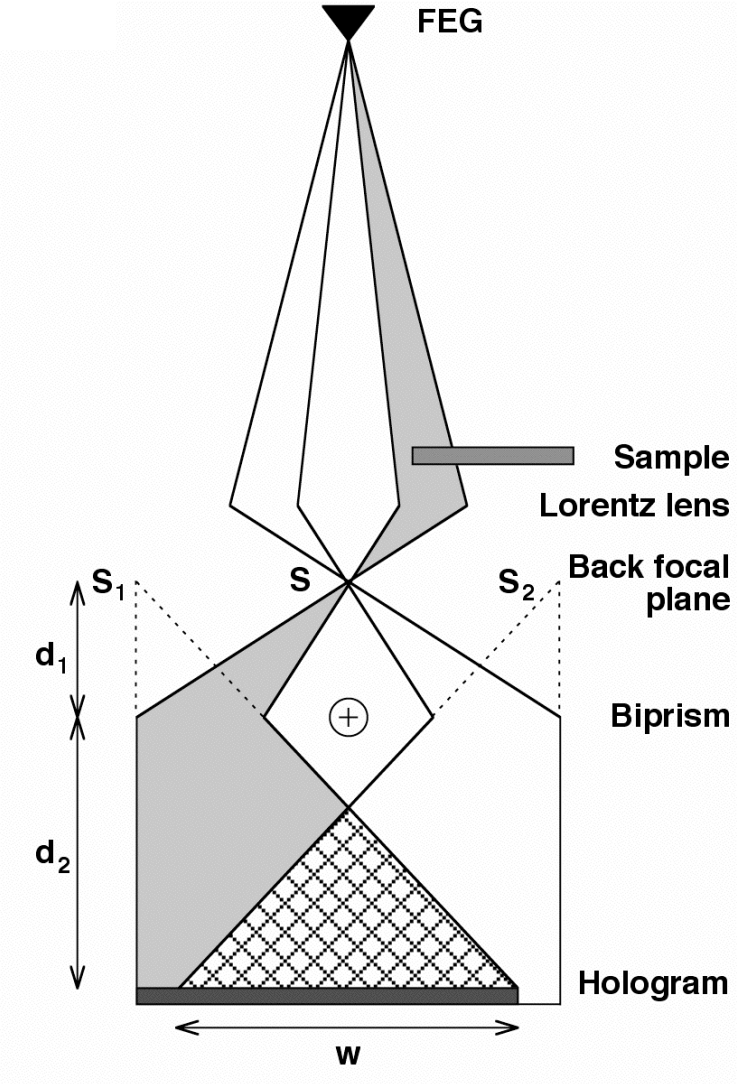

- If α is the deflection angle introduced by a biprism of radius **R** and λ is the wavelength of the illumination then:
- the overlap width

$$w = 2\left(\frac{d_1 + d_2}{d_1}\right)\left(\alpha \frac{d_1 d_2}{d_1 + d_2} - R\right)$$

- the interference fringe spacing

$$s = \lambda\left(\frac{d_1 + d_2}{2\alpha d_1}\right)$$

- the total number of interference fringes is proportional to the square of the biprism voltage.

Off-axis electron holography

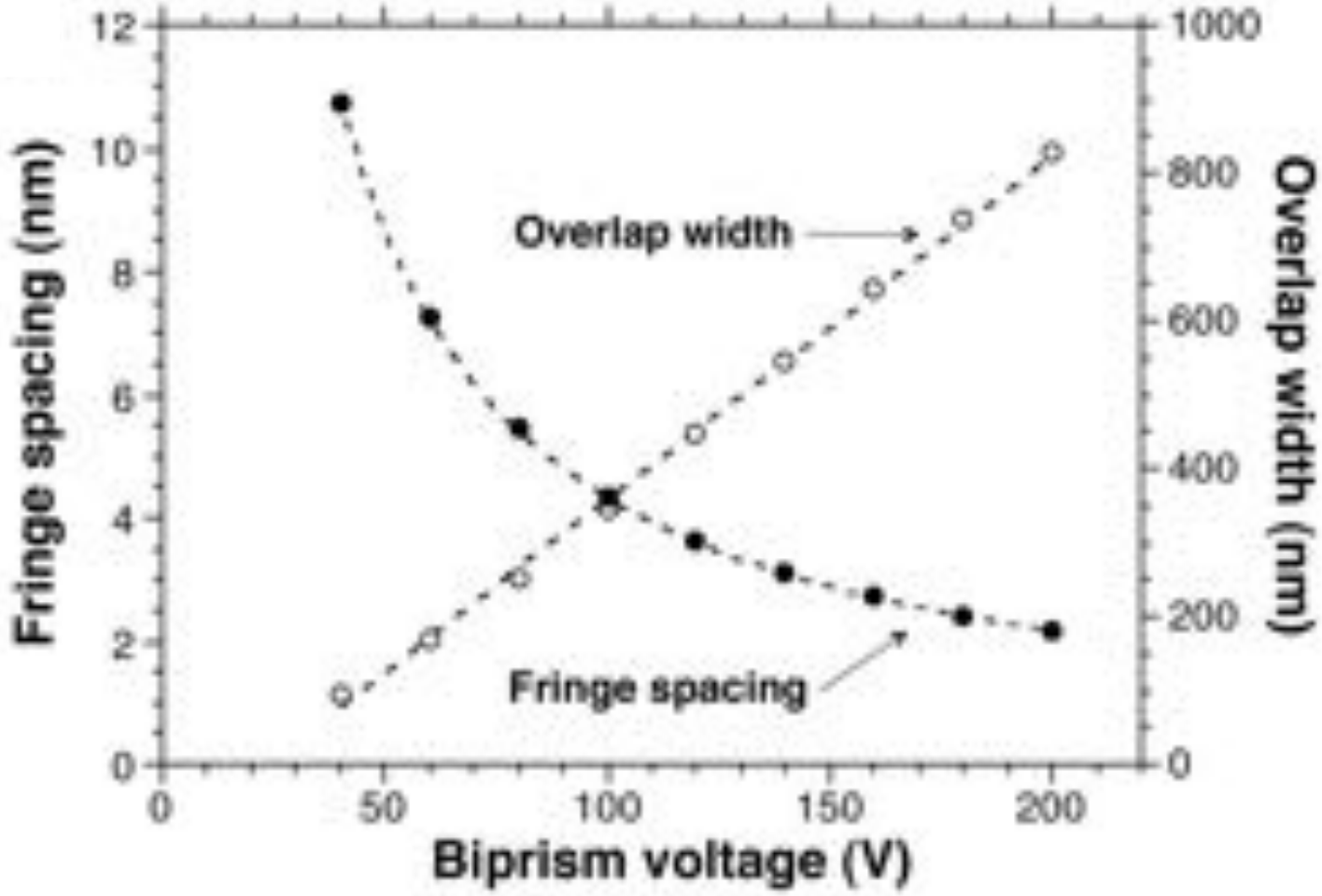

Off-axis electron holography

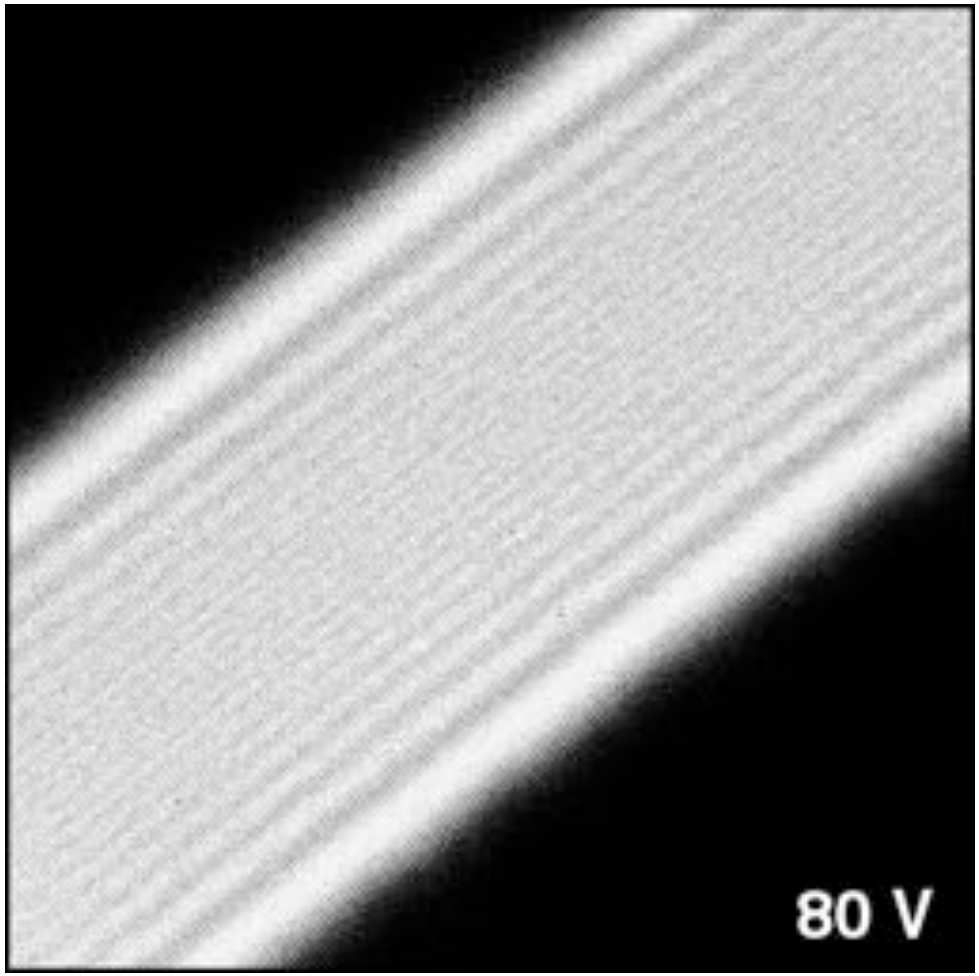

Acknowledgment: M. R. McCartney

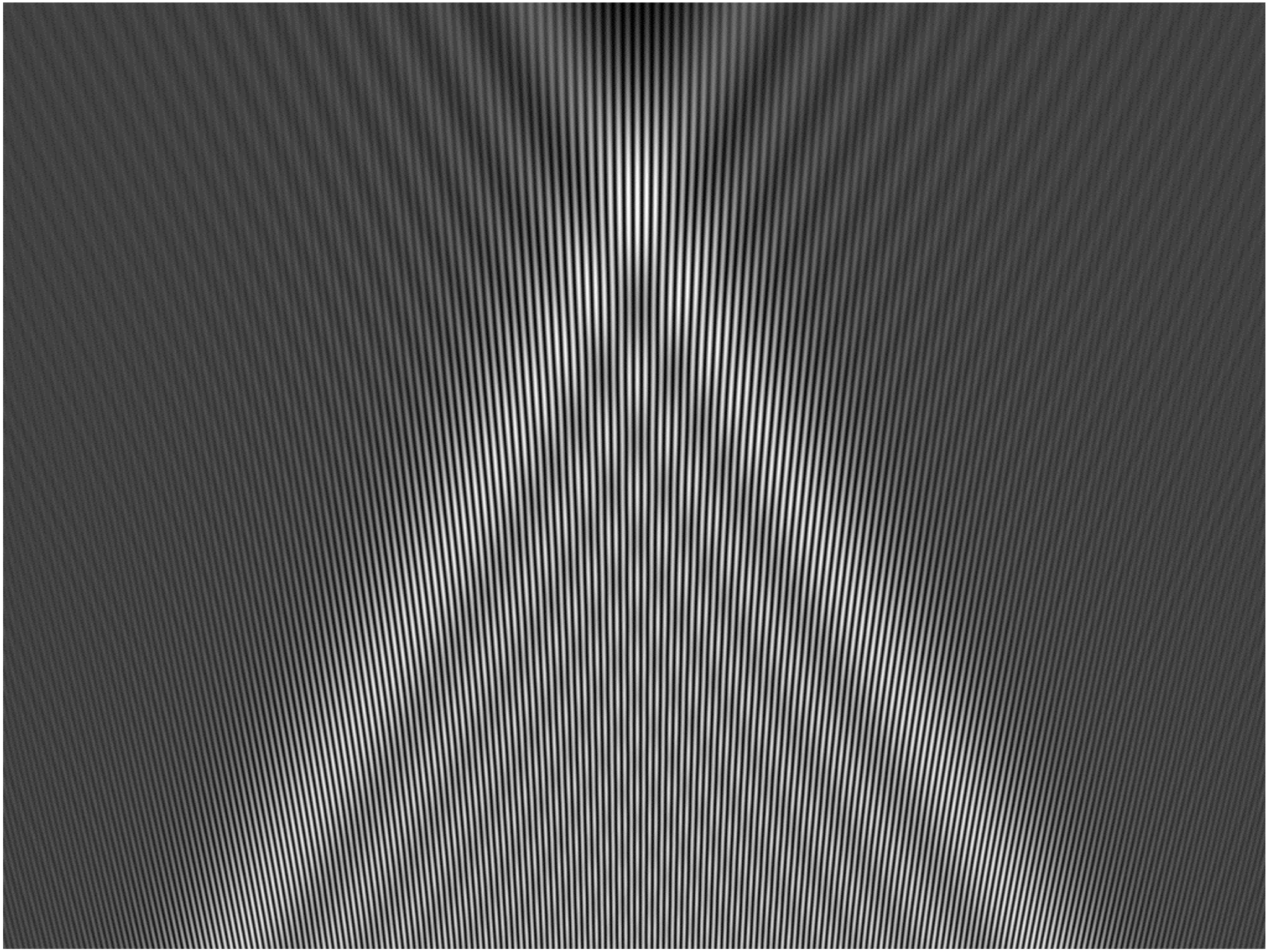

Basis of off-axis electron holography

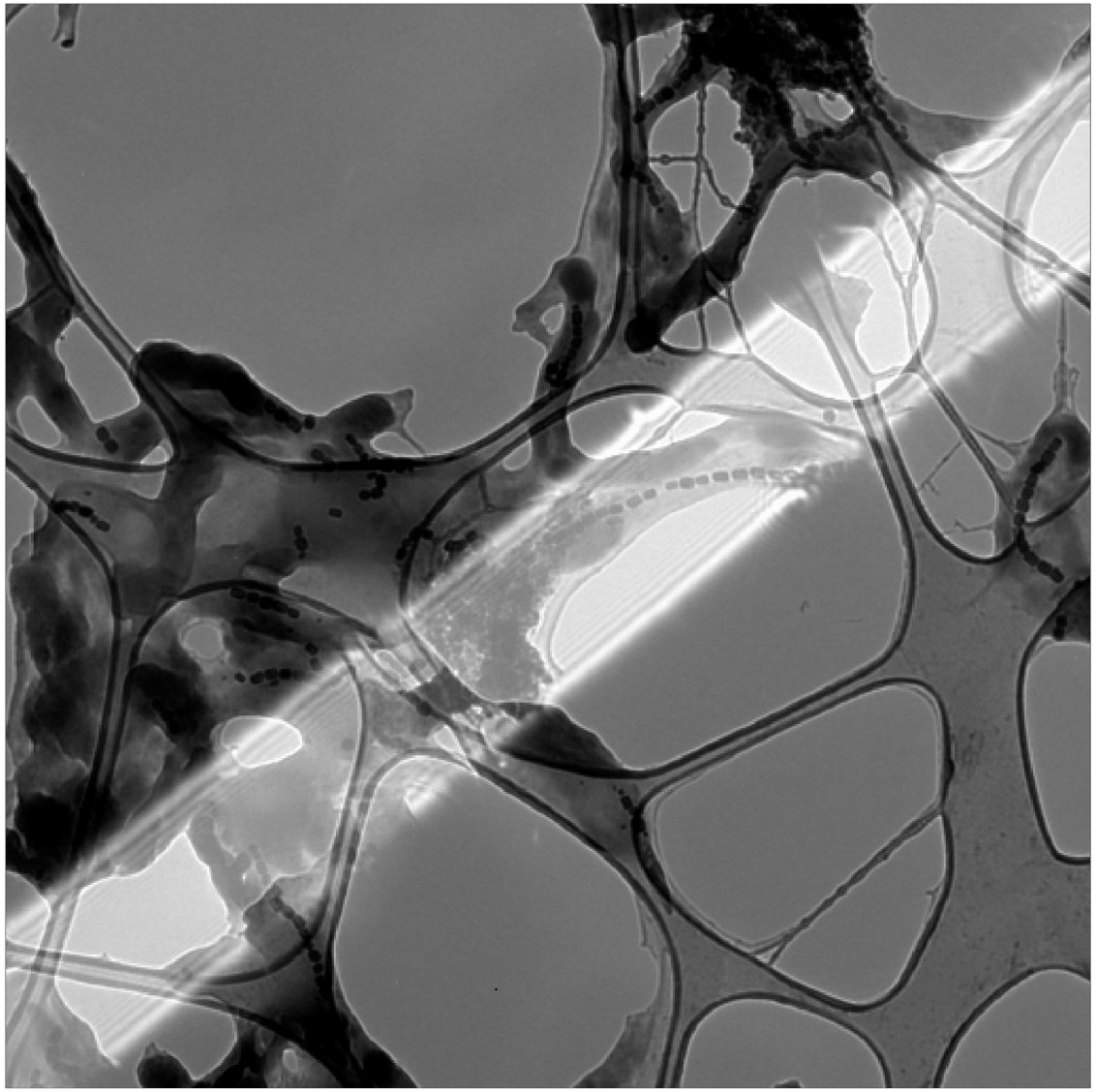

Off-axis electron hologram of magnetic nanocrystals

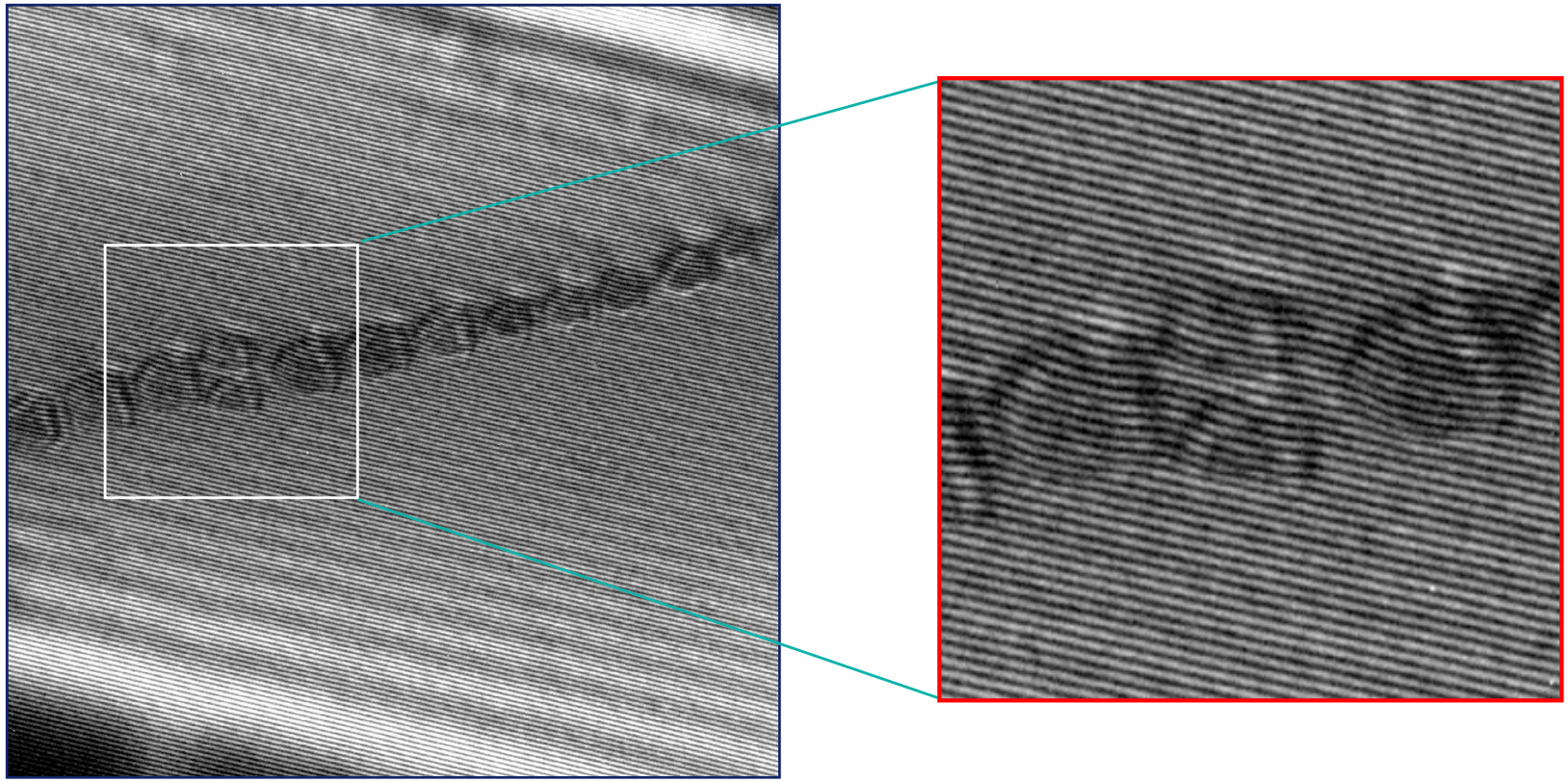

Electron hologram acquired in magnetic-field-free conditions
3.9 nm interference fringe spacing

Off-axis electron holography: digital reconstruction

Off-axis electron hologram from thin crystal showing interference fringes within sample

Phase image obtained from inverse Fourier transform of one 'sideband' selected from Fourier transform of hologram

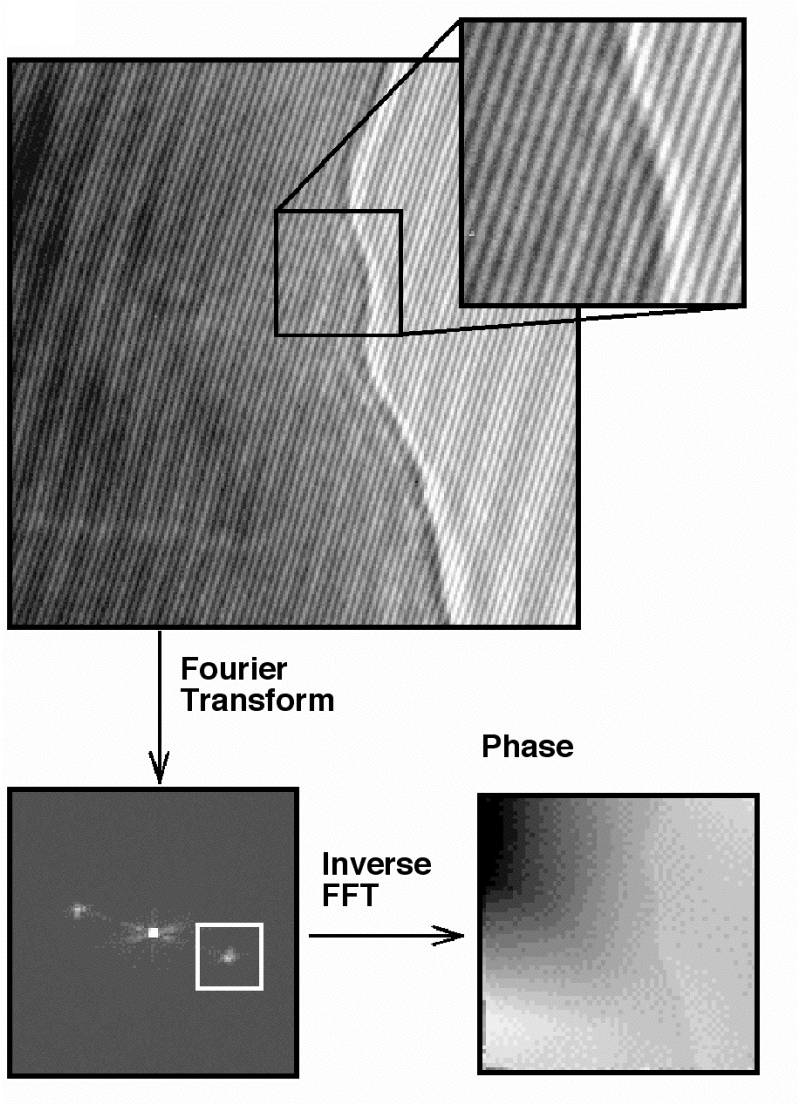

Acknowledgment: M. R. McCartney

Off-axis electron holography

Conventional bright-field TEM:

$$\psi_i(\mathbf{r}) = A_i(\mathbf{r})\exp[i\phi_i(\mathbf{r})]$$

$$I(\mathbf{r}) = \left|A_i(\mathbf{r})\right|^2$$

Off-axis electron holography:

$$I_{hol}(\mathbf{r}) = \left|\psi_i(\mathbf{r}) + \exp[2\pi i\mathbf{q_c}\bullet\mathbf{r}]\right|^2$$

$$I_{hol}(\mathbf{r}) = 1 + A_i^2(\mathbf{r}) + 2A_i(\mathbf{r})\cos[2\pi i\mathbf{q_c}\bullet\mathbf{r} + \phi_i(\mathbf{r})]$$

$$FT[I_{hol}(\mathbf{r})] = \delta(\mathbf{q}) + FT[A_i^2(\mathbf{r})] + \delta(\mathbf{q}+\mathbf{q_c})\otimes FT[A_i(\mathbf{r})\exp[i\phi_i(\mathbf{r})]] + \delta(\mathbf{q}-\mathbf{q_c})\otimes FT[A_i(\mathbf{r})\exp[-i\phi_i(\mathbf{r})]]$$

$$A = \sqrt{\mathrm{Re}^2 + \mathrm{Im}^2} \qquad \phi = \tan^{-1}\left(\frac{\mathrm{Im}}{\mathrm{Re}}\right)$$

Fundamentals of electron interference

Basis of off-axis electron holography

Each electron travels as a wave but interacts with the detector as a particle

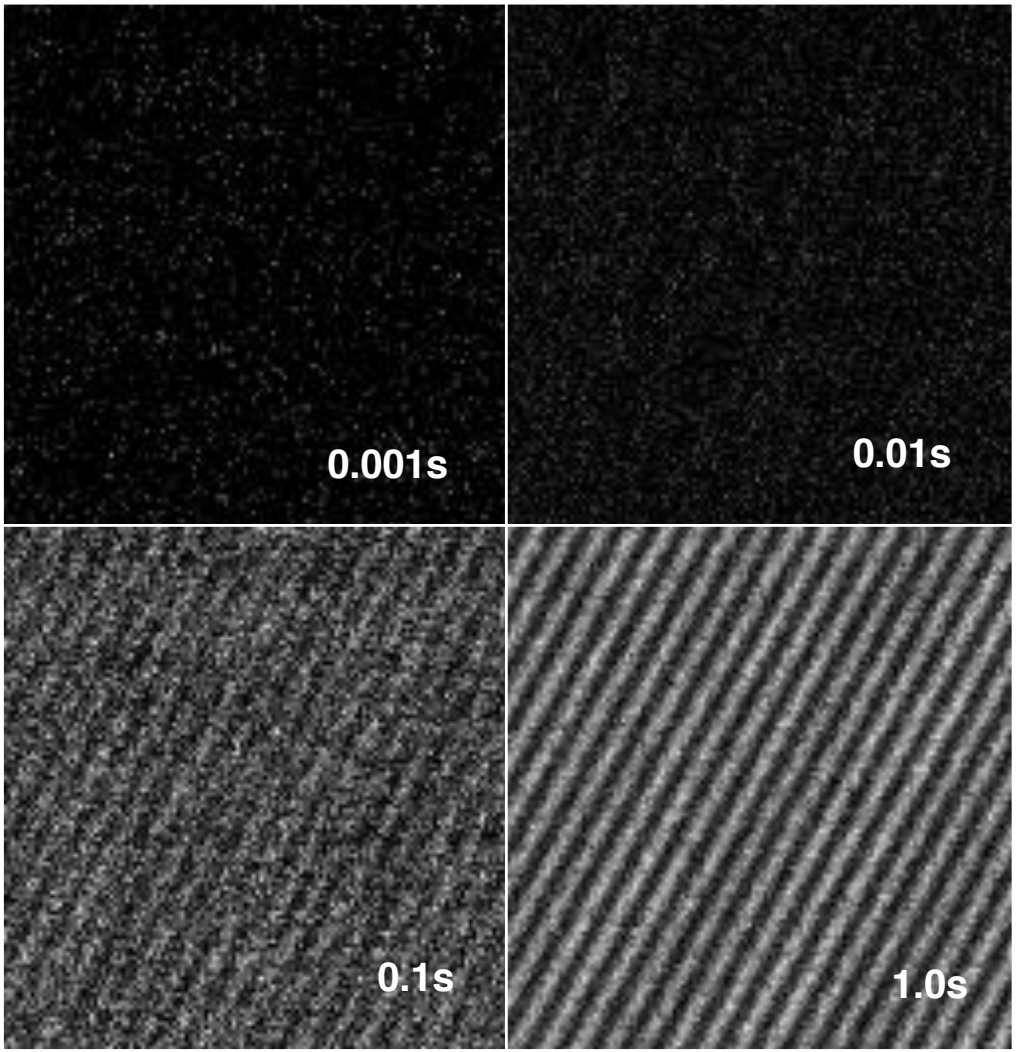

Acknowledgment: M. R. McCartney

The most beautiful experiment in physics

Electron holography of magnetic fields

Off-axis electron holography of magnetic materials

1965 Akira Tonomura works on field emission electron sources and pioneers the characterization of magnetic materials using electron holography.

Hitachi Advanced Research Laboratory

Off-axis electron holography of magnetic materials

'Optical' reconstruction of electron holograms

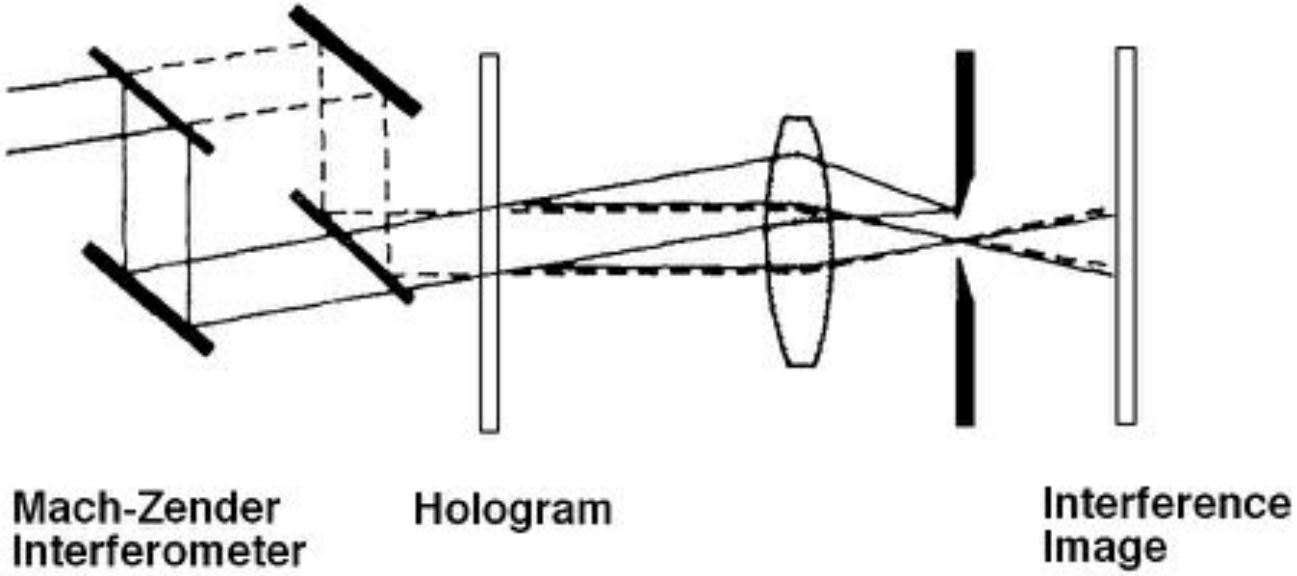

Acknowledgment: A. Tonomura

Off-axis electron holography of magnetic materials

55-nm-thick plate-shaped
{111} Co particle

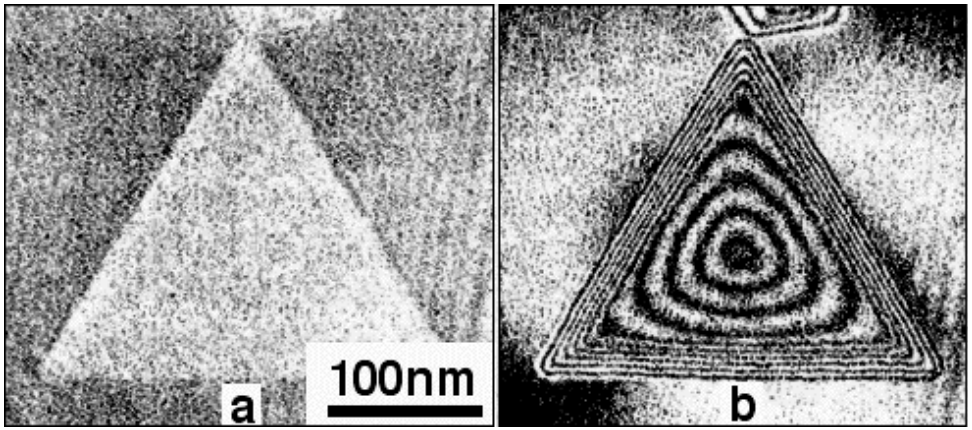

2 times phase amplified
interference micrograph

Phys. Rev. Lett. 44, 1430 (1980)

Acknowledgment: A. Tonomura

Off-axis electron holography of magnetic materials

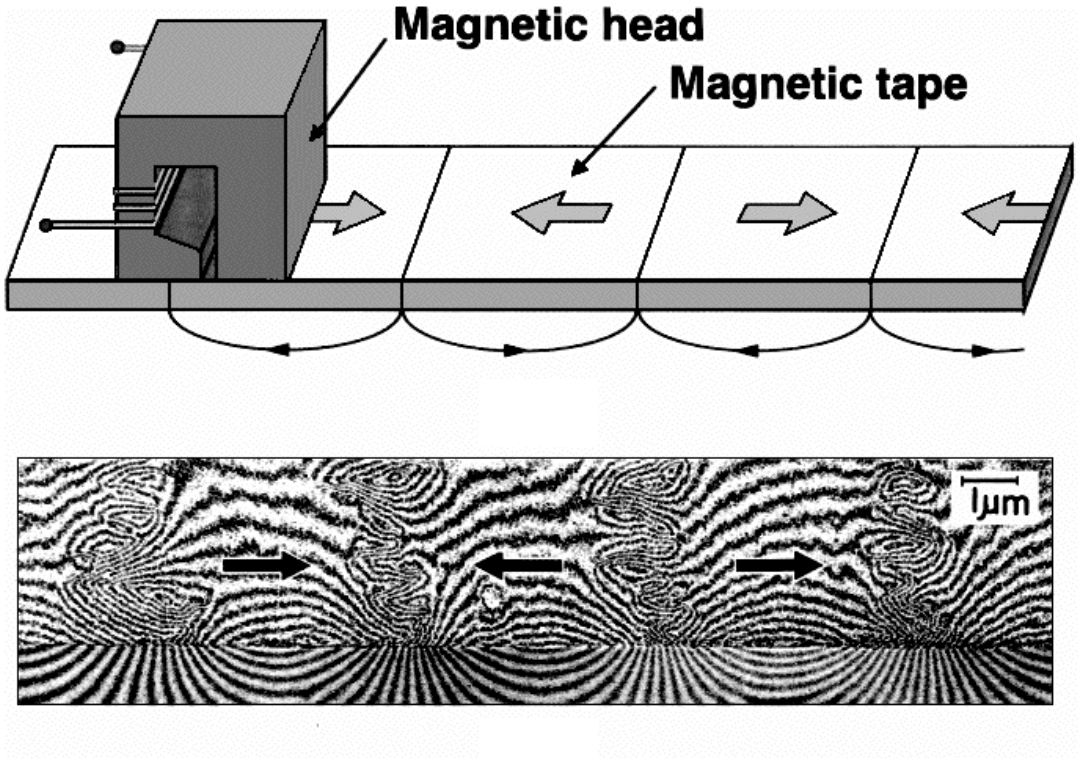

45-nm-thick recorded Co film with 5 μm bit length

Appl. Phys. Lett. 42, 746 (1983)

Acknowledgment: A. Tonomura

Off-axis electron holography of magnetic materials

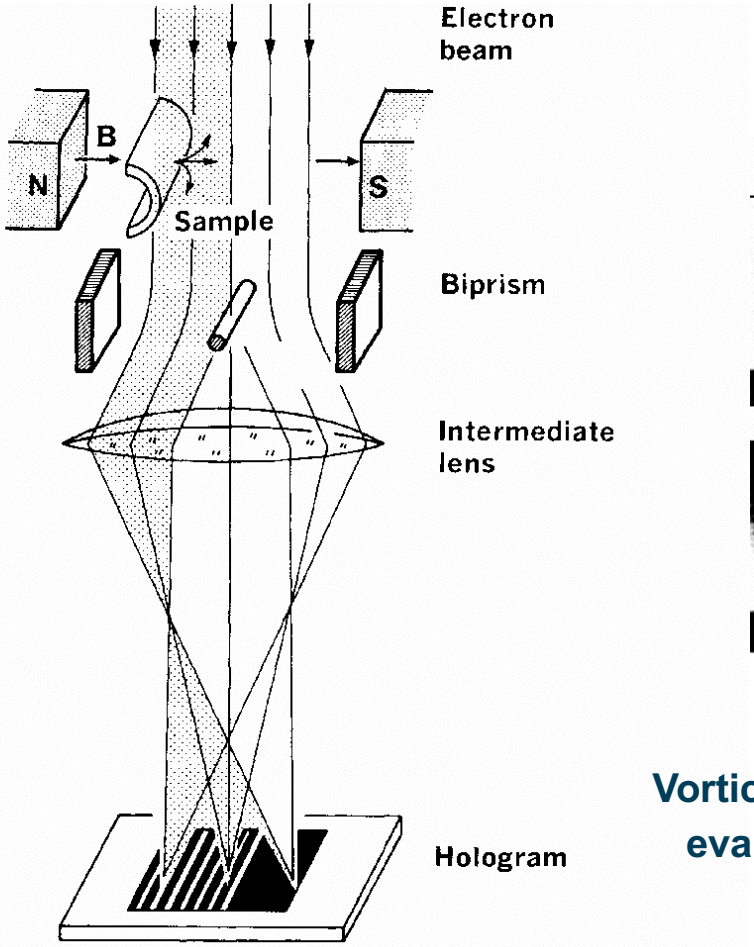

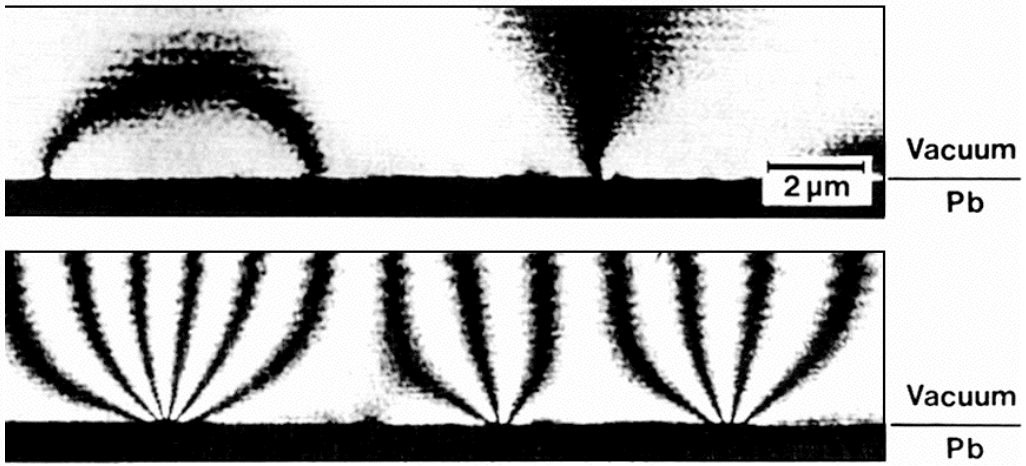

Vortices in superconducting Pb films (0.2 and 1 μm thick) evaporated onto W wire. Holograms recorded at 4.5K.

Phys. Rev. Lett. 62, 2519 (1989)

Acknowledgment: A. Tonomura

Off-axis electron holography of magnetic materials

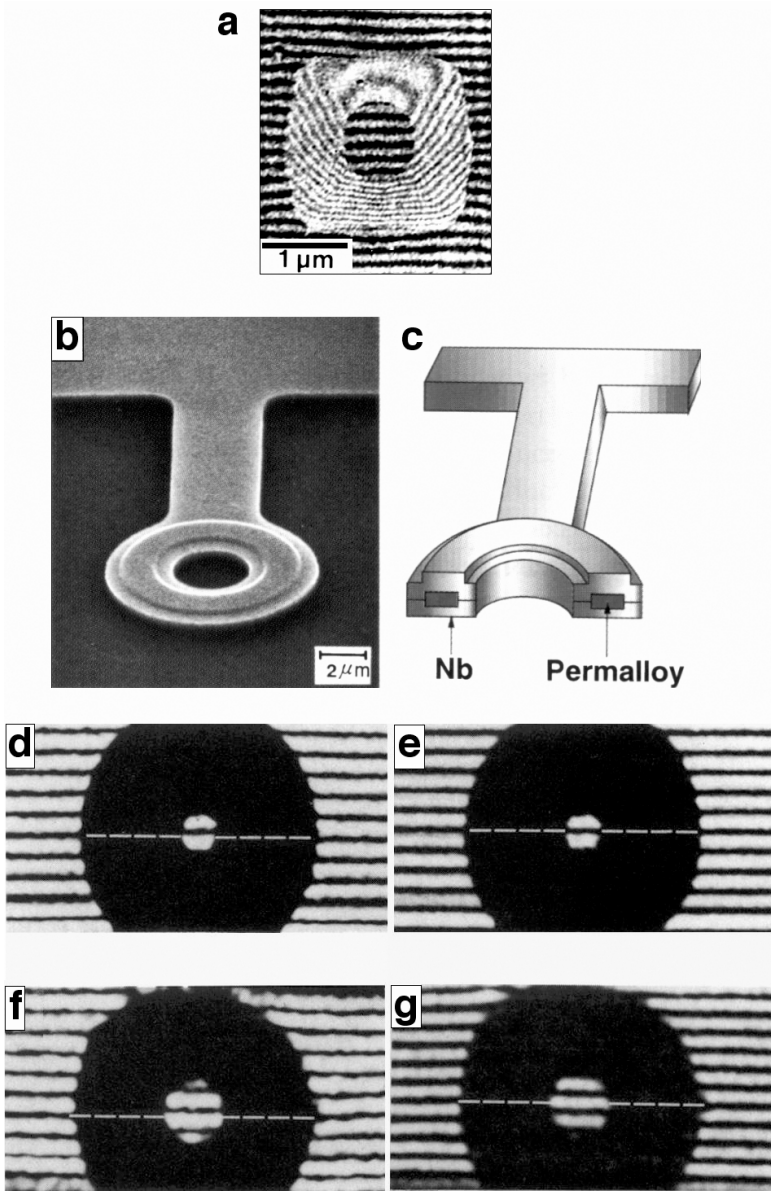

Interferogram of a toroidal 40 nm thick film of permalloy.

SEM image and schematic diagram of permalloy toroid covered with superconducting Nb.

Interferograms: (d) and (e) are for a toroid in which the magnetic flux is quantized below T_c in units of $n(h/2e)$, where n is even. For (f) and (g), n is odd. For (d) and (f), T = 15 K, whereas for (e) and (g) T = 5 K (phase amplification x 1).

Phys. Rev. Lett. 48, 1443 (1982).

Phys. Rev. A 34, 815 (1986).

Acknowledgment: A. Tonomura

Magnetic fields: digital analysis

Off-axis electron holography of magnetic materials

Lorentz (Fresnel underfocus) image of $Nd_2Fe_{14}B$.

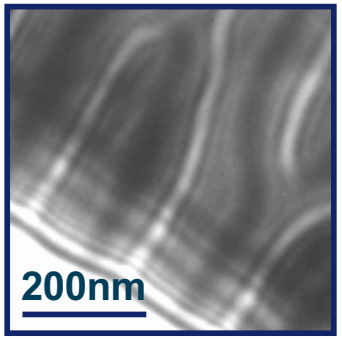

Phase

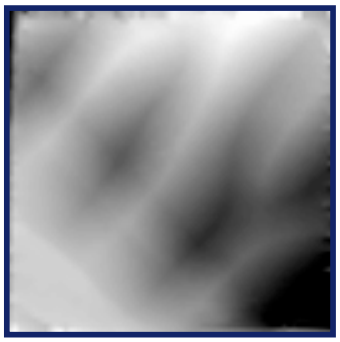

Contoured phase

x-differential

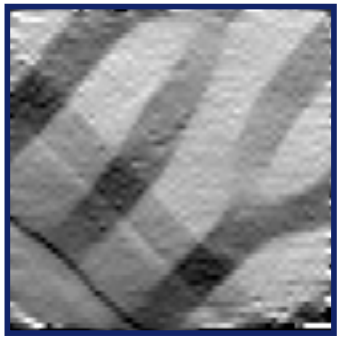

y-differential

Acknowledgment: M. R. McCartney and Y. Zhu

Off-axis electron holography of magnetic materials

Vector map

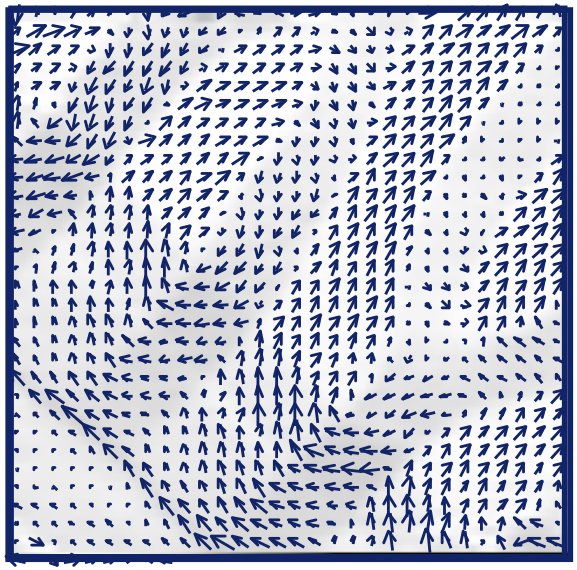

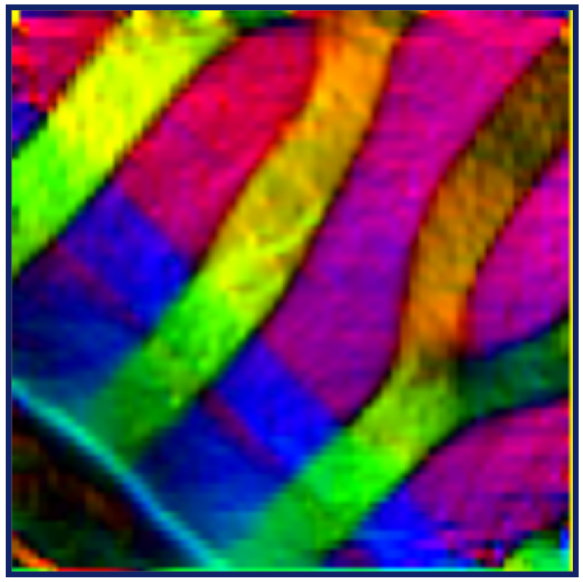

Color map

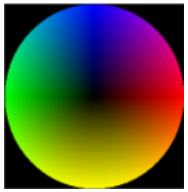

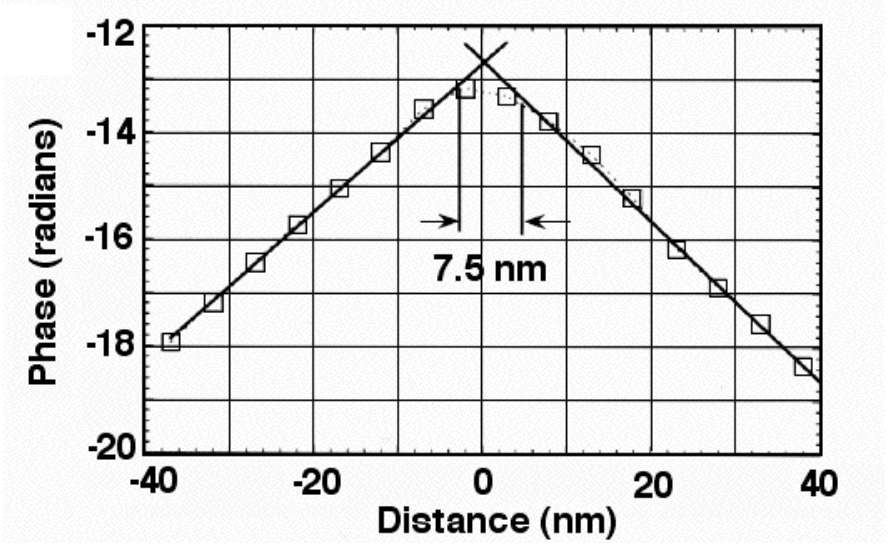

Linescan obtained from the phase image across a 90° domain wall.

The line profile provides an upper limit for the domain wall width of 10 nm.

Appl. Phys. Lett. 72, 1380 (1998).

Acknowledgment: M. R. McCartney and Y. Zhu

Magnetic fields in nanoscale materials

Off-axis electron holography of magnetic materials

Cobalt nanoparticle rings

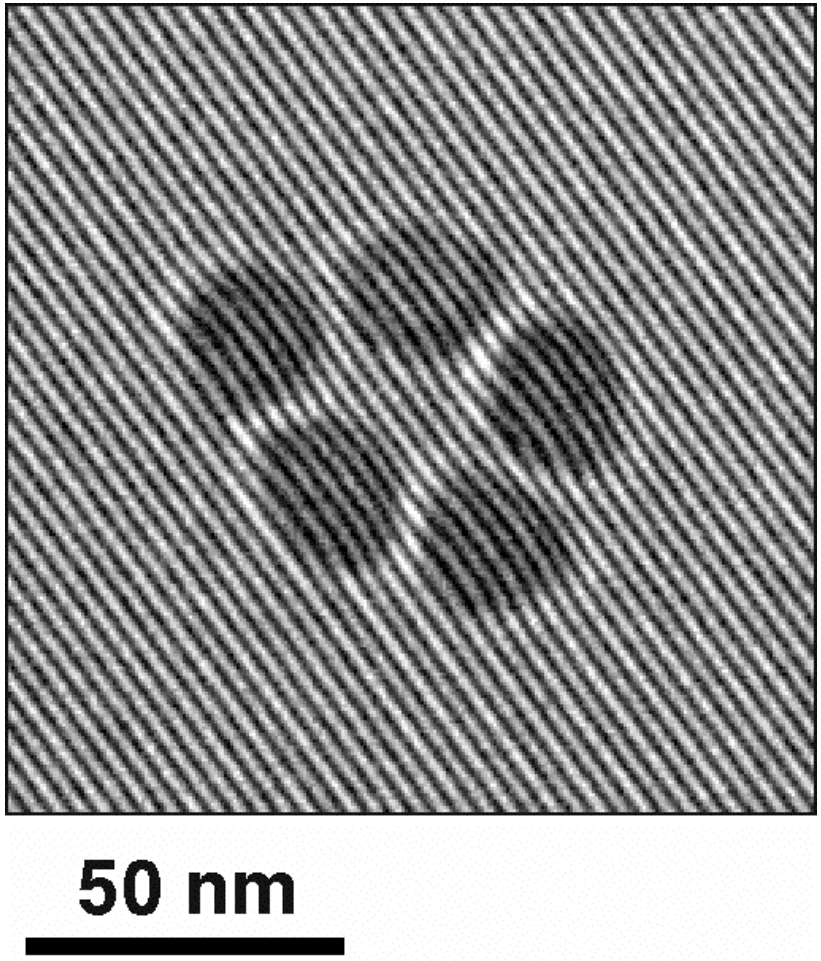

Acknowledgment: Alexander Wei

Off-axis electron holography of magnetic materials

Cobalt nanoparticle rings

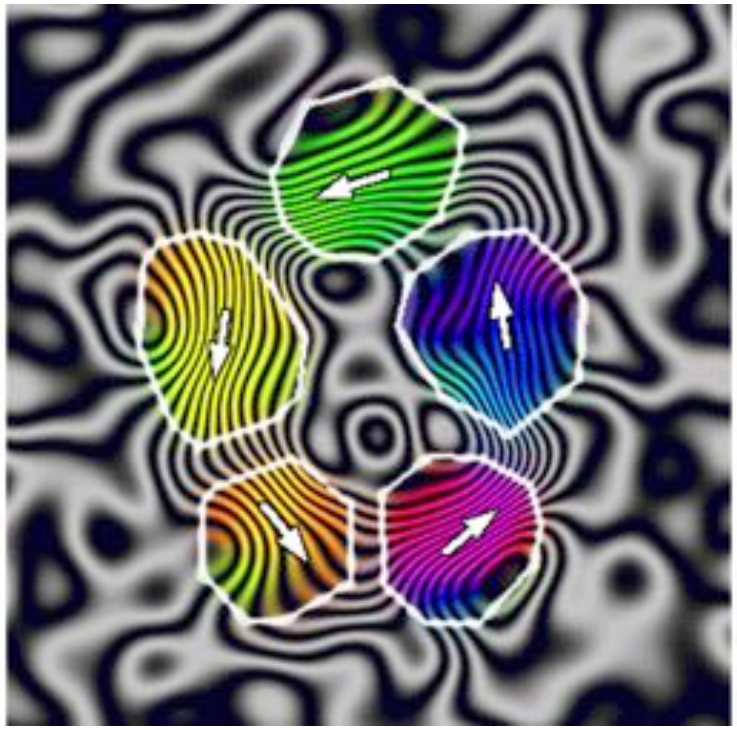

Acknowledgment: Alexander Wei

Determination of coercivity of remananence by applying successive increasing OOP fields.

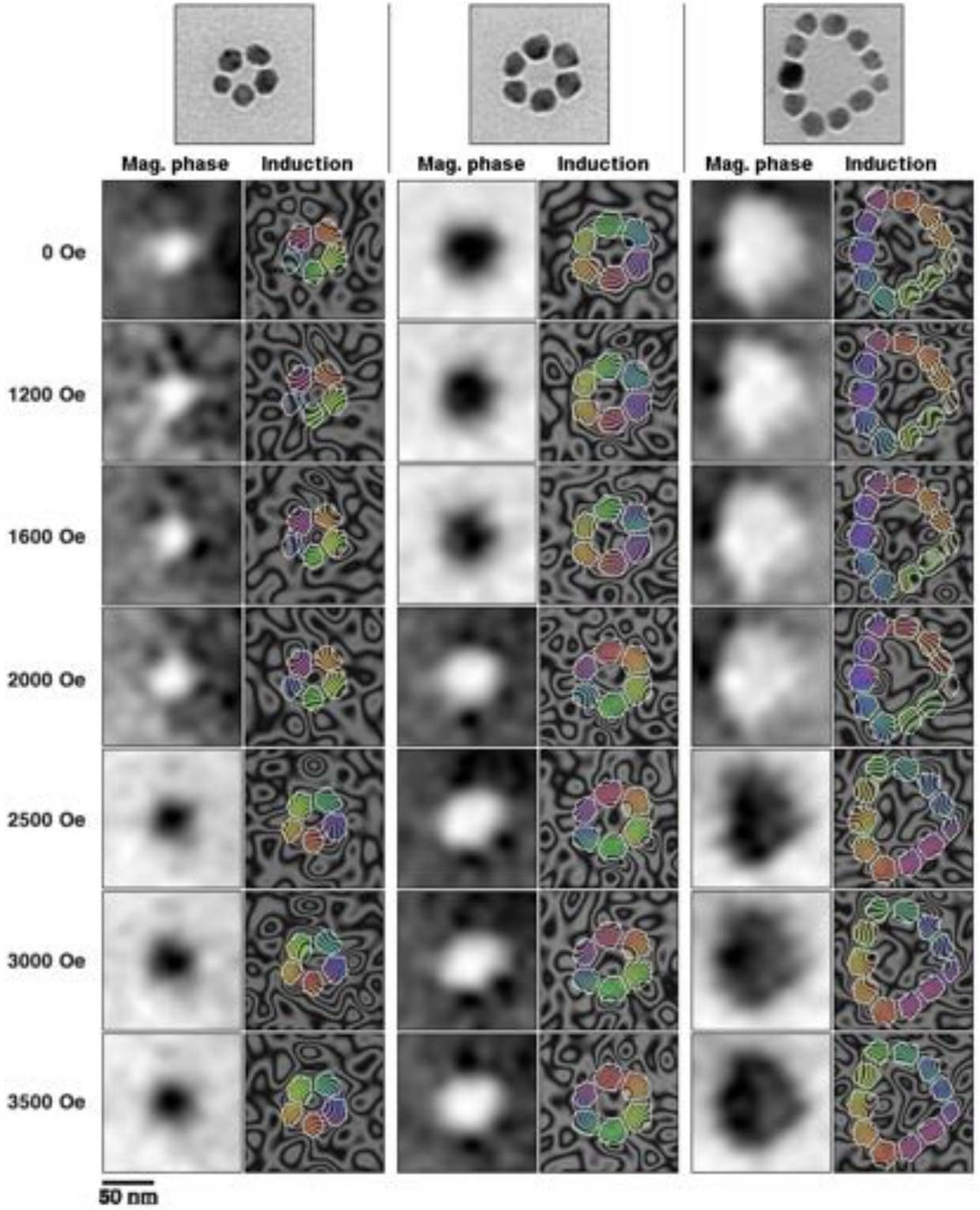

Magnetic fields: some theoretical background

Off-axis electron holography of magnetic materials

The difference between the magnetic contribution to the phase shift at any two points is:

$$\Delta\phi_m = \phi_m(x_1, y_1) - \phi_m(x_2, y_2) = -\frac{e}{\hbar}\int_{-\infty}^{+\infty} A_z(x_1, y_1, z)\,dz + \frac{e}{\hbar}\int_{-\infty}^{+\infty} A_z(x_2, y_2, z)\,dz$$

For a rectangular loop formed by two parallel electron trajectories crossing the sample at these points and joined, at infinity, by segments perpendicular to the trajectories:

$$\Delta\phi_m = -\frac{e}{\hbar}\oint \mathbf{A}\cdot d\mathbf{l}$$

Using Stokes' theorem:

$$\Delta\phi_m = \frac{e}{\hbar}\iint \mathbf{B}\cdot\hat{\mathbf{n}}\,dS = \frac{\pi}{\phi_0}\Phi(S)$$

where $\varphi_0 = h/2e = 2.07\times10^{15}$ Tm^2 is a flux quantum.

Off-axis electron holography of magnetic materials

The relationship between the magnetic contribution to the phase shift and the magnetic induction can be established from the gradient of φ_m

$$\vec{\nabla}\phi_m(x,y) = \frac{e}{\hbar}\left[B_y^p(x,y)\ ,\ -B_x^p(x,y)\right]$$

where $$B_j^p(x,y) = \int_{-\infty}^{+\infty} B_j(x,y,z)\,dz$$ **are the components of the magnetic induction perpendicular to the electron beam direction projected in the beam direction**

In the special case when (i) stray fields surrounding the sample can be neglected, (ii) the sample has a constant thickness and (iii) the magnetic induction does not vary with z within the specimen:

$$\vec{\nabla}\phi_m(x,y) = \frac{et}{\hbar}\left[B_y(x,y)\ ,\ -B_x(x,y)\right]$$

The separation of electrostatic and magnetic contributions to the phase shift is almost always mandatory in order to obtain quantitative magnetic information from a phase image. The few instances when this extra step may be avoided include the special case of magnetic domains in a thin film of constant thickness.

Quantitative magnetic measurements

- Magnetization
- Coercivity
- Magnetic moment
- Critical sizes for SPM/ SD/ PSD/ MD transitions
- Effects on magnetic microstructure of interactions, shape and crystallography

Electron holography of magnetite nanocrystals at elevated temperature

Off-axis electron holography at elevated temperature

Fe_3O_4 grain heated to 550 °C and cooled to room temperature

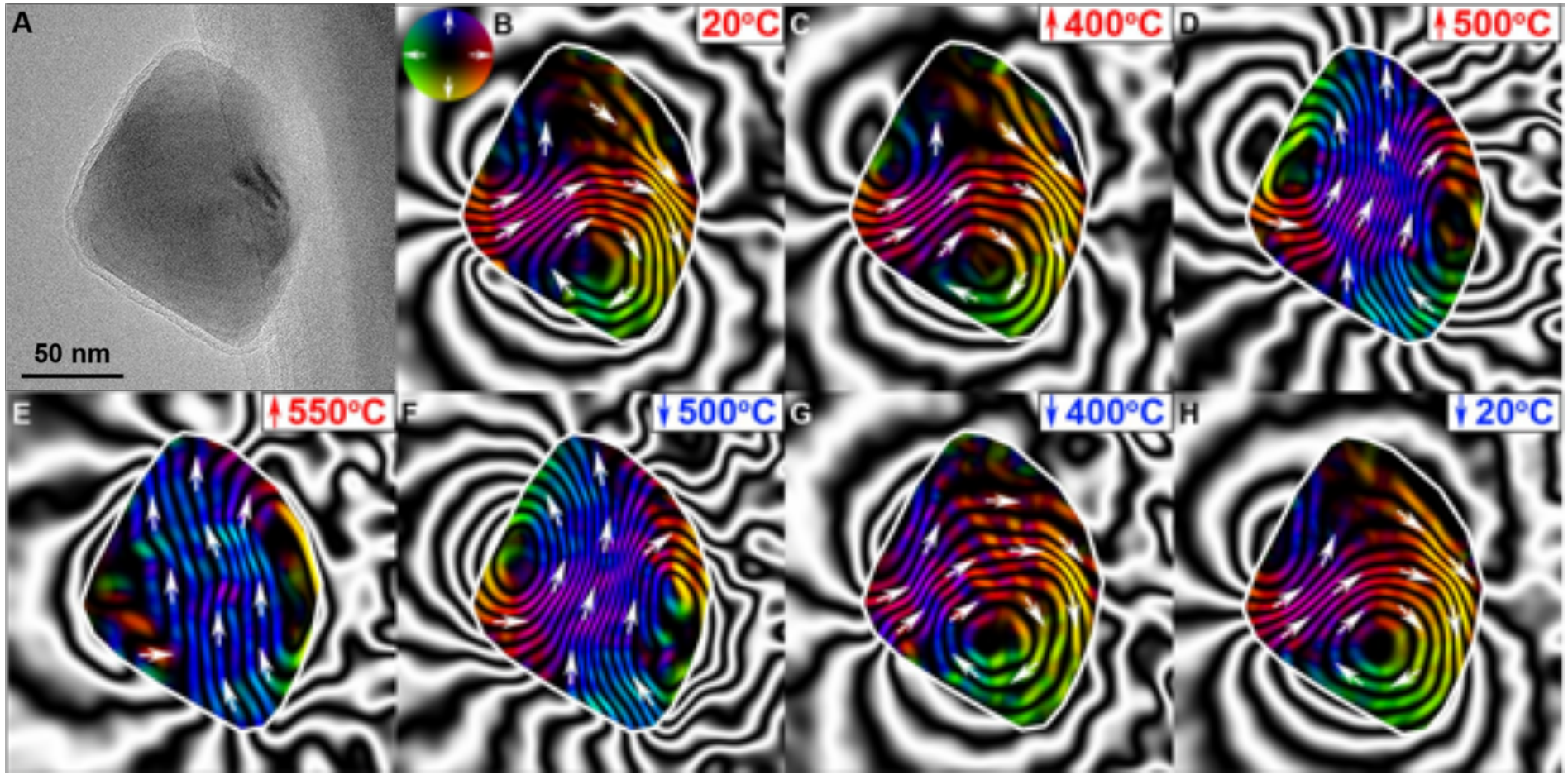

T. Almeida, A. Muxworthy, W. Williams

Electron holography at elevated temperature

Fe_3O_4 grain heated to 600 °C and cooled to room temperature

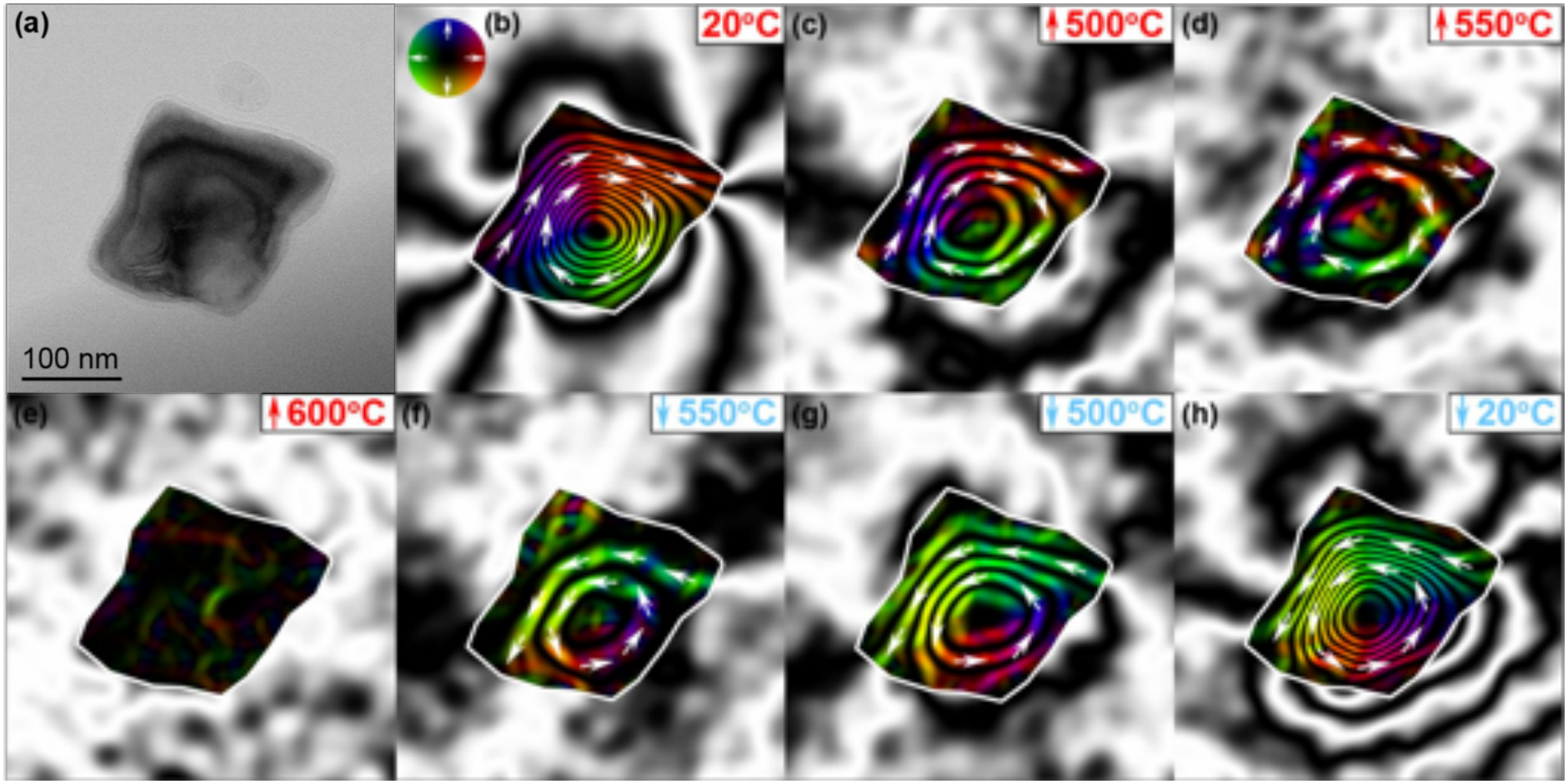

T. Almeida, A. Muxworthy, W. Williams

Influence of reactive gas

In situ gas reaction experiments at elevated temperature

250 x 150 nm Fe_3O_4 particle before *in situ* oxidation

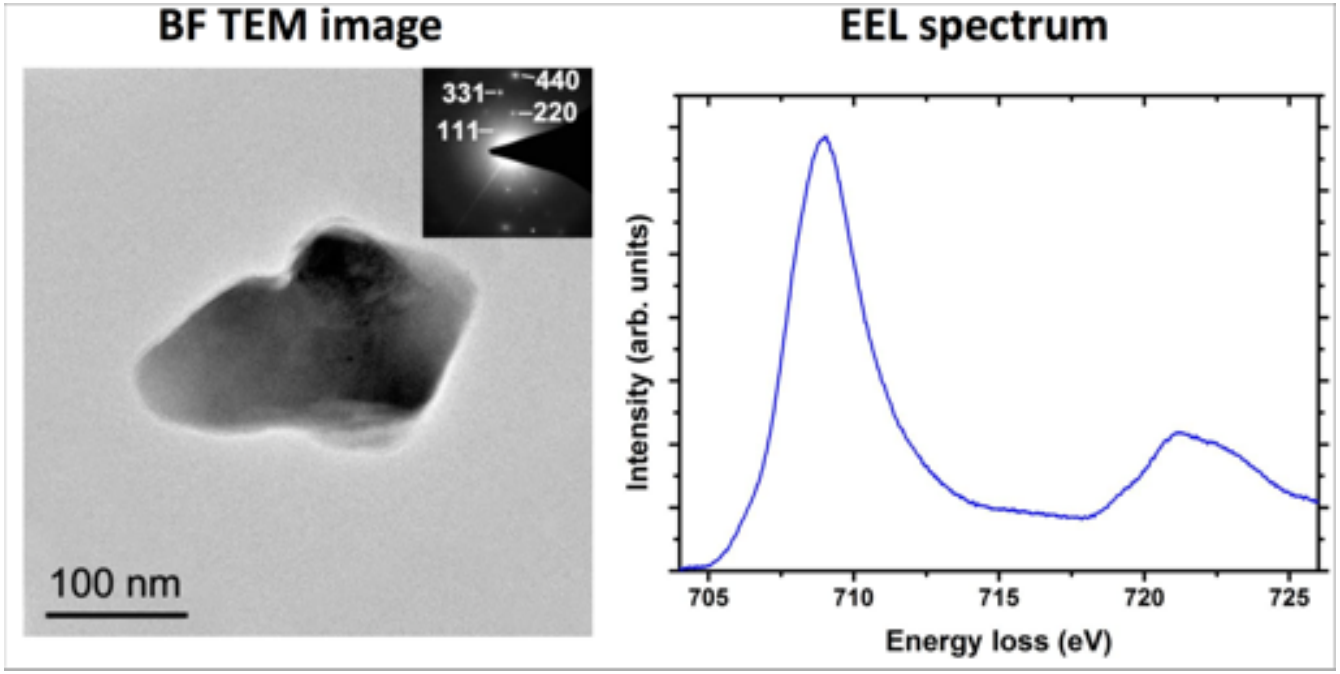

After heating at 700 °C in 9 mbar O_2 for 8 hours

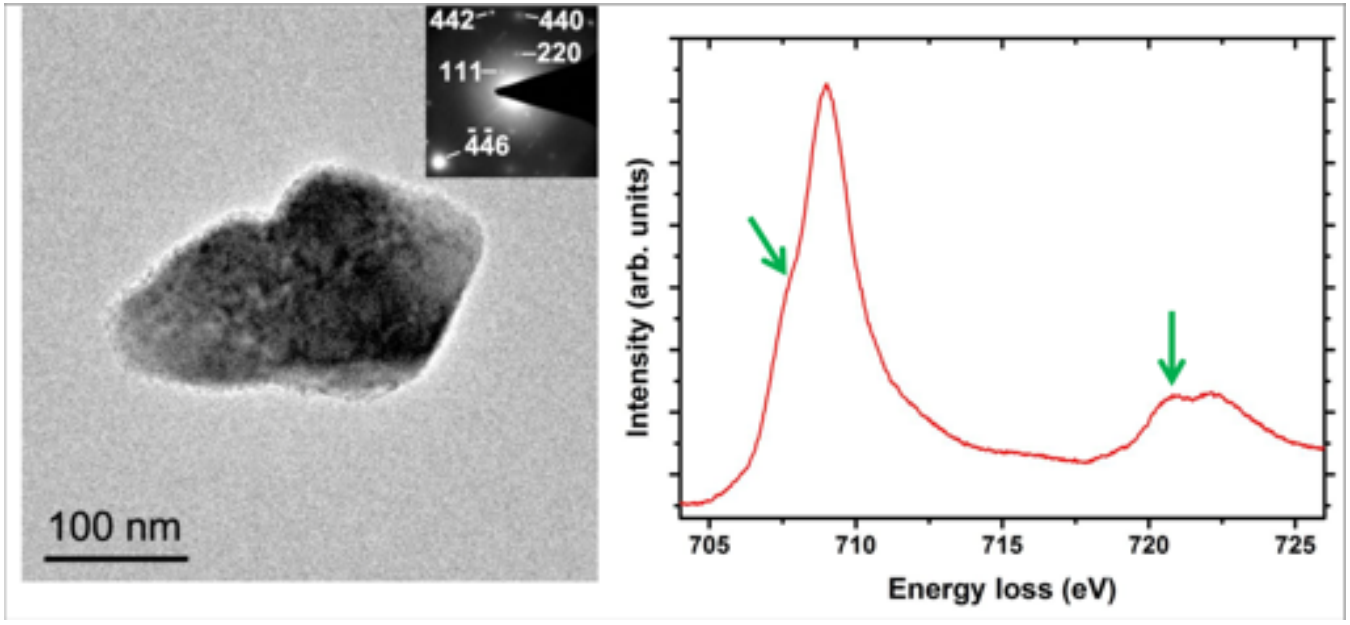

In situ heating in oxygen

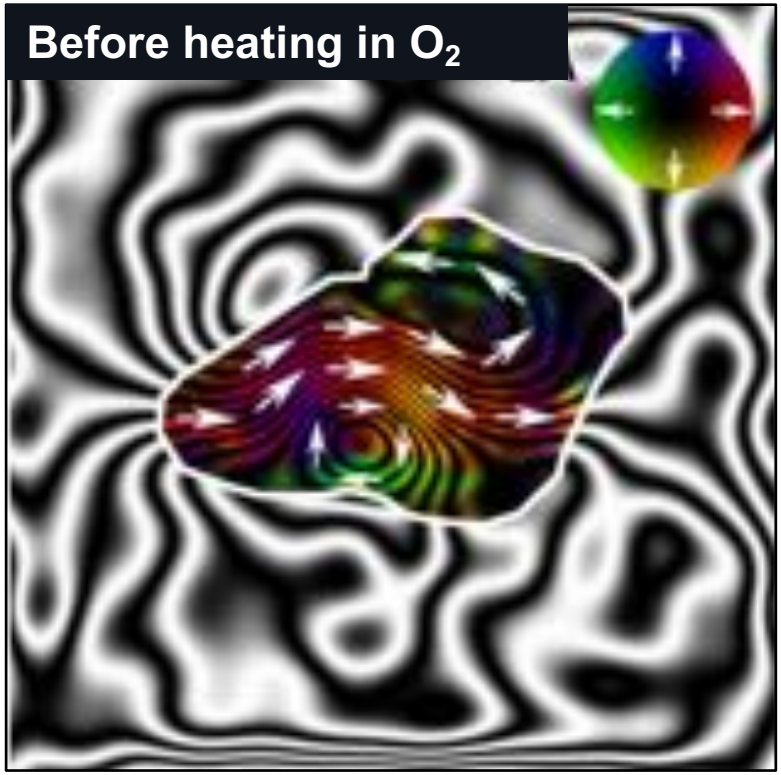

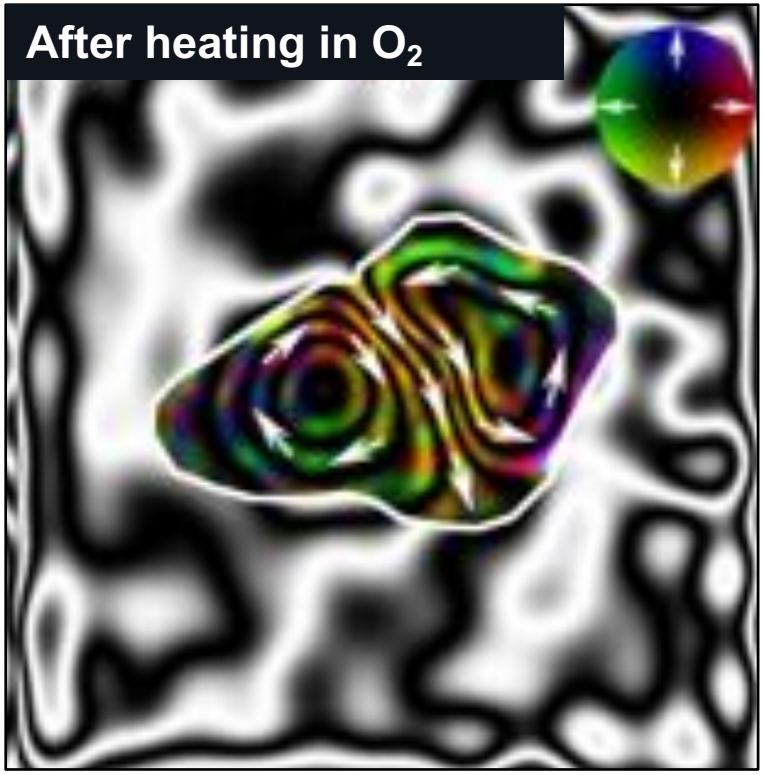

Bright-field TEM images and magnetic induction maps of an elongated 250 nm Fe_3O_4 particle acquired before and after *in situ* heating to 700 °C in 9 mbar of O_2 in the TEM.

Magnetic skyrmions

Magnetic skyrmions

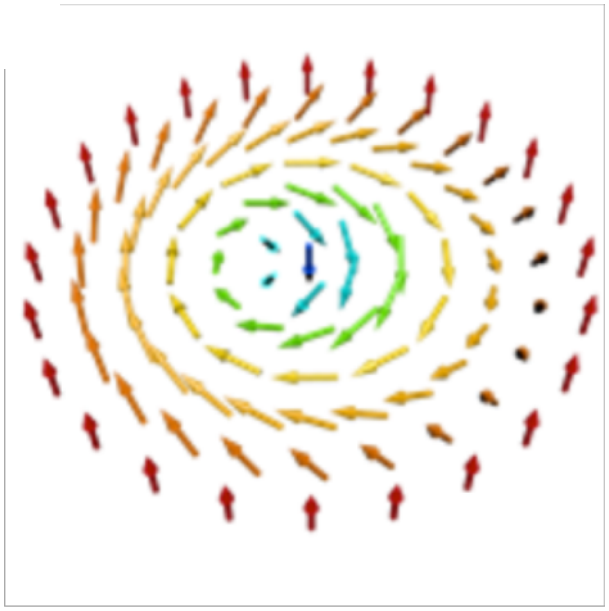

Spin configuration of a Bloch-type skyrmion.

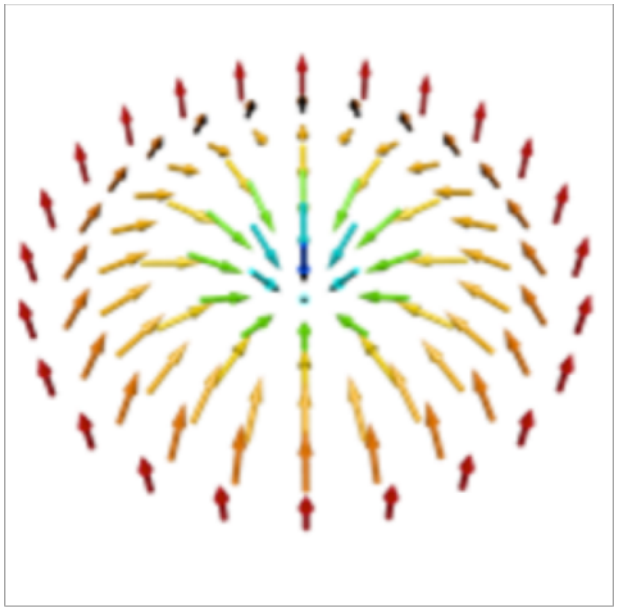

Spin configuration of a Néel-type skyrmion.

Magnetic skyrmions

Schematic B-T phase diagram for magnetic skyrmions in B20 FeGe

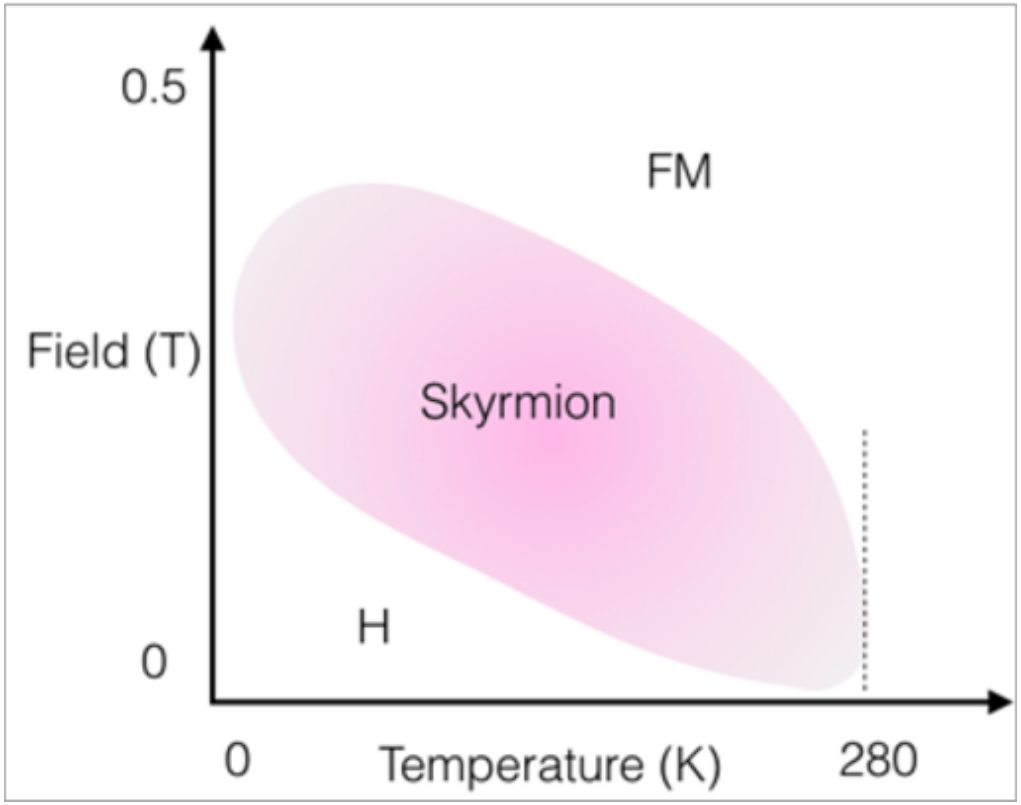

Regions “H”, “Skyrmion” and “FM” denote a helical structure, a skyrmion lattice and a saturated ferromagnetic state, respectively. The critical temperature is 278.3 K.

Skyrmions in FeGe

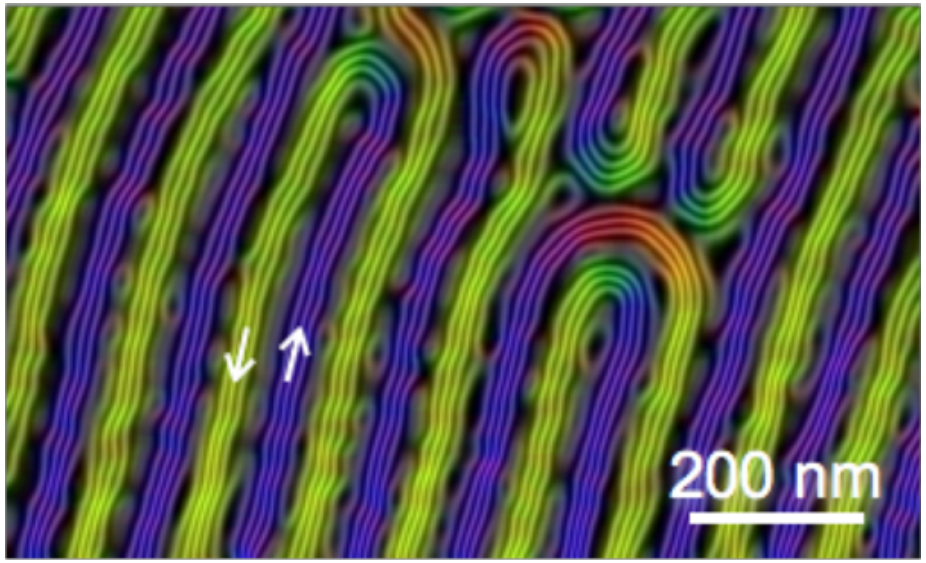

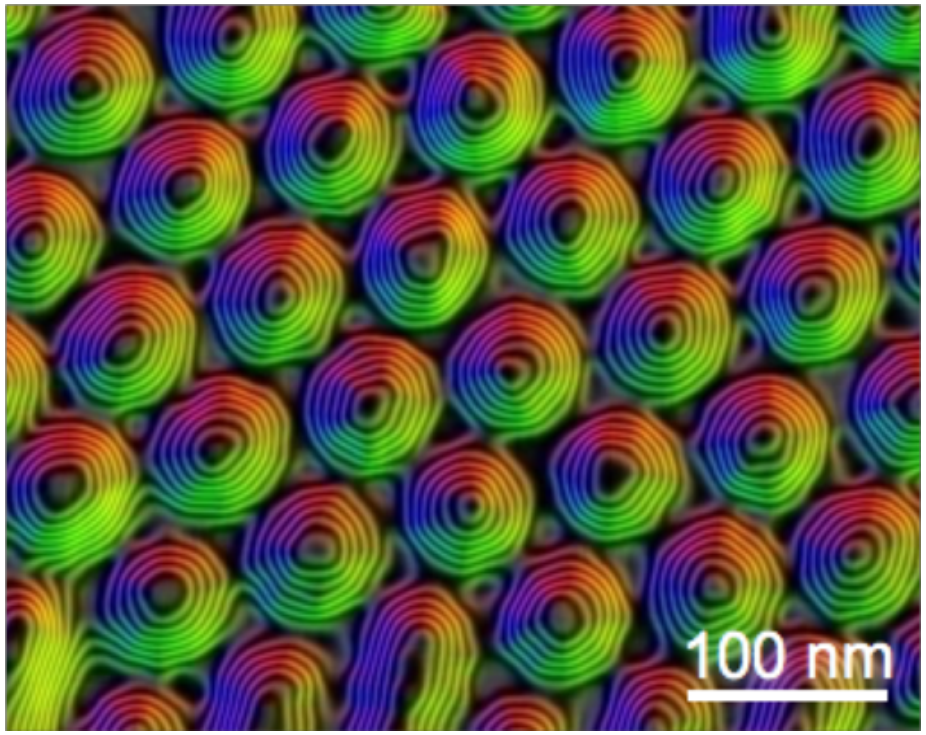

Magnetic induction maps of helical structures and a skyrmion lattice recorded in out-of-plane magnetic fields of 0 and 100 mT at 200 K. The contour spacing is 0.098 rad.

Kiyou Shibata,
Yoshinori Tokura

Magnetic skyrmions in FeGe

Magnetic field dependence of skyrmions in FeGe.

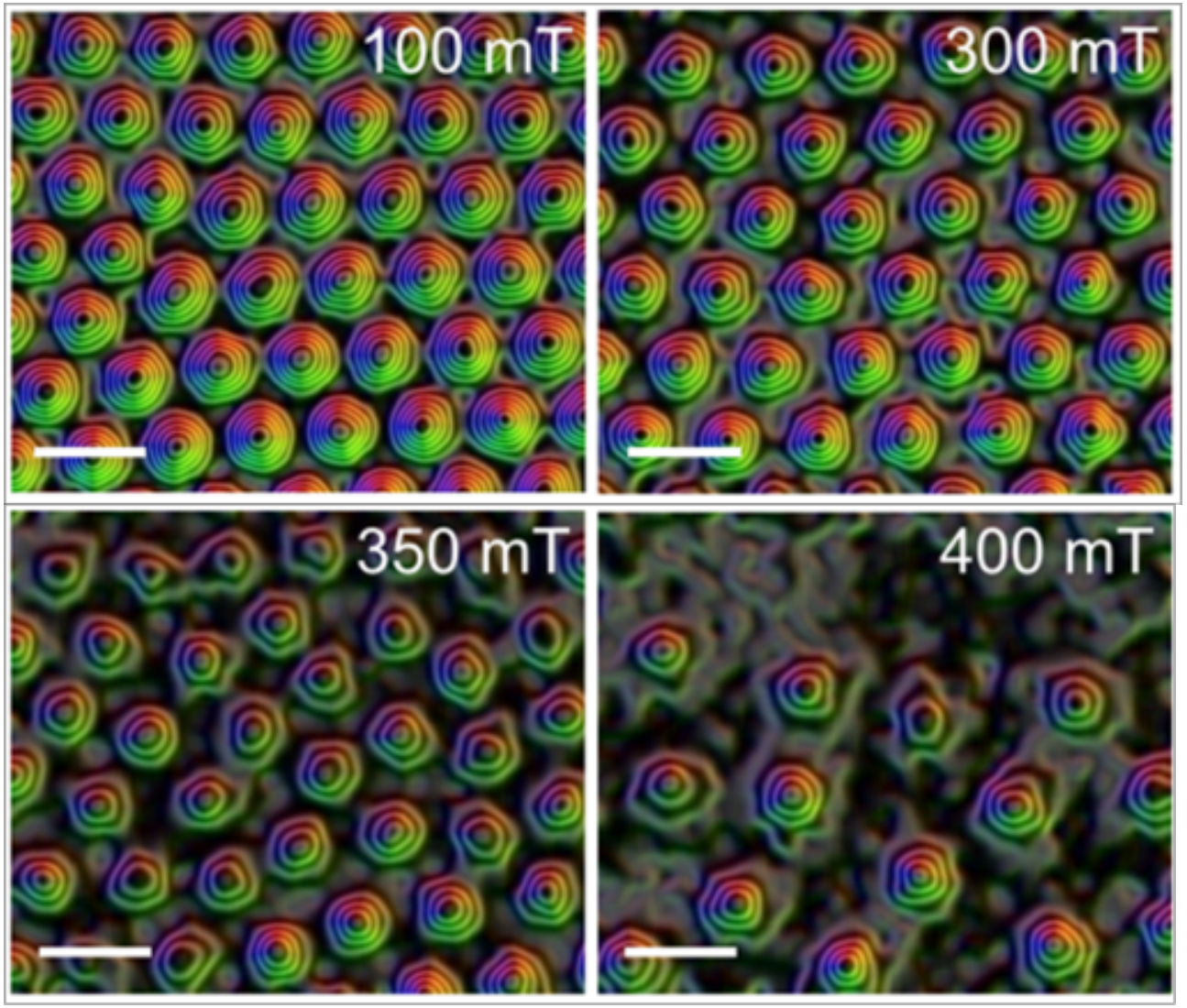

Kiyou Shibata,
Yoshinori Tokura

Magnetic induction maps of a skyrmion lattice recorded at 200 K in the indicated out-of-plane magnetic fields. The contour spacing is 0.098 radians.

Skyrmions in confined geometries

Magnetic skyrmions in FeGe

TEM sample preparation by FIB milling

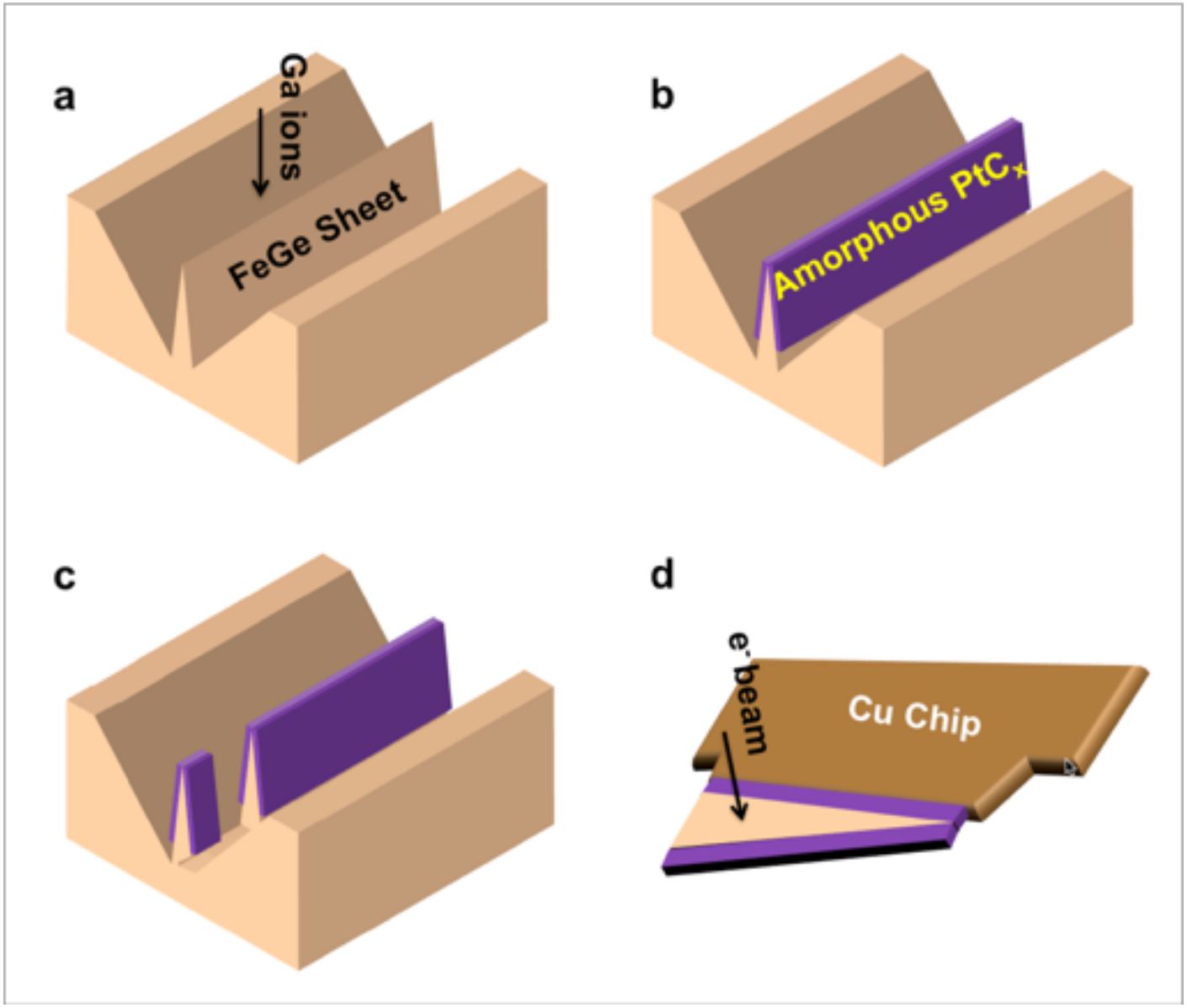

Skyrmions in FeGe

Magnetic field dependence at 220 K after zero field cooling

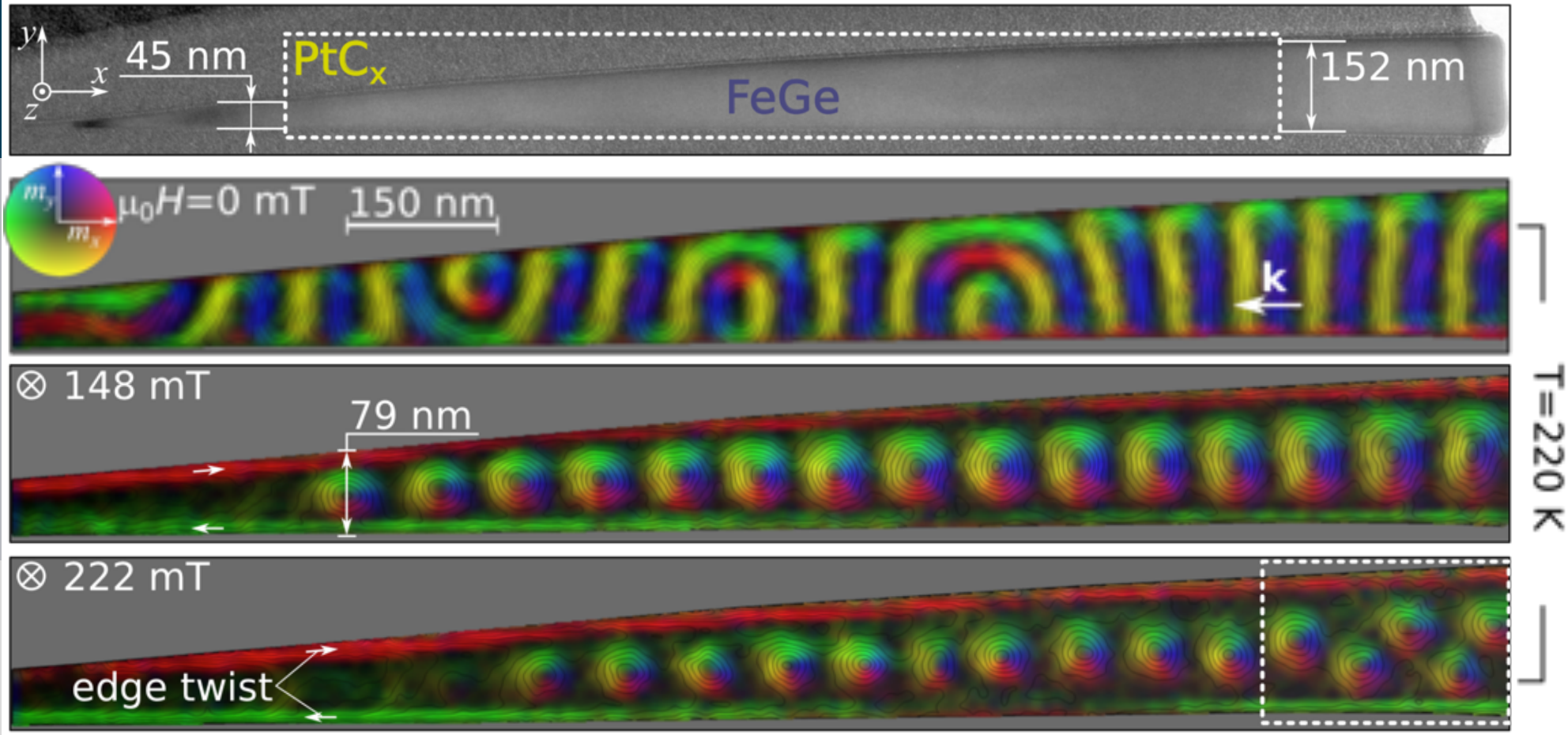

Hai-Feng Du

Magnetic skyrmions in FeGe

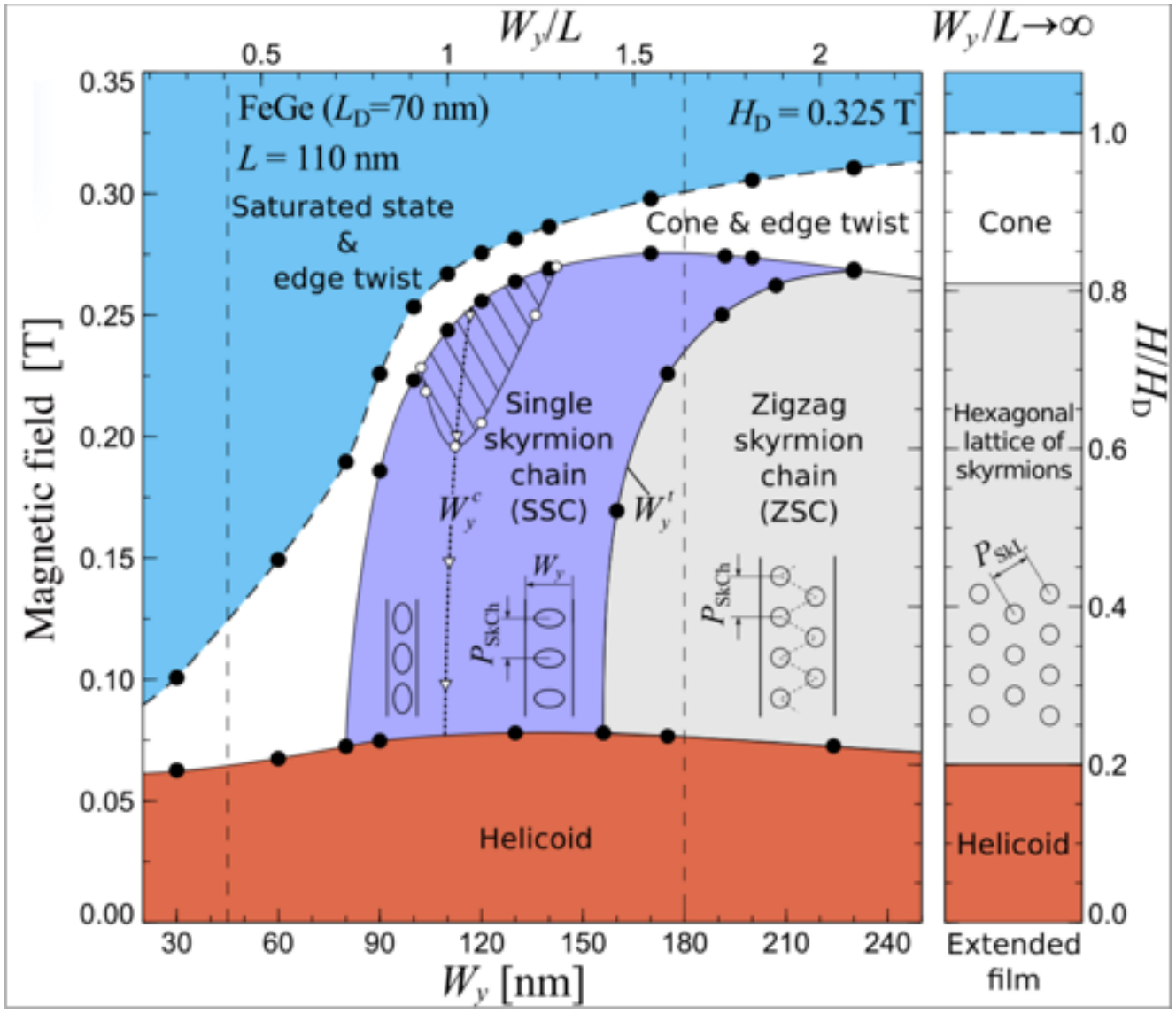

Phase diagram of skyrmions in a nansotripe of B20-FeGe determined from both experimental results and simulations. W_y is the width of the sample and L is its thickness.

Off-axis electron holography of electrostatic potentials

Electrostatic contribution to phase shift

Phase shift:

$$\phi(x,y) = C_E \int_{z=-\infty}^{z=+\infty} V(x,y,z)\,dz$$

Sensitive to:

- composition
- density
- bonding/ ionicity
- electrostatic fields at depletion layers
- electrostatic fringing fields outside materials

The mean inner potential

Mean inner potential contribution to phase shift

Mean inner potential:

$$V_0 = \left(\frac{1}{\Omega}\right)\int_{\Omega} V(x,y,z)\,dxdydz = \left(\frac{h^2}{2\pi me\Omega}\right)\sum_{\Omega} f_{el}(0)$$

Ω = unit cell volume. $f_{el}(0)$ = electron scattering factor at zero scattering angle.

Mean inner potential contribution to phase shift if there is no variation in V_0 in the electron beam direction:

$$\phi(x) = C_E V_0(x) t(x) \qquad C_E = \left(\frac{2\pi}{\lambda}\right)\left(\frac{E+E_0}{E(E+2E_0)}\right)$$

V_0 measured using electron holography from specimens of known geometry typically:

- **12 V for Si and 22-24 V for Fe**
- **10 - 15% lower than values calculated using neutral atom scattering factors**

Mean inner potential contribution to phase shift

HR image of a cuboctahedral ZrO_2 particle.

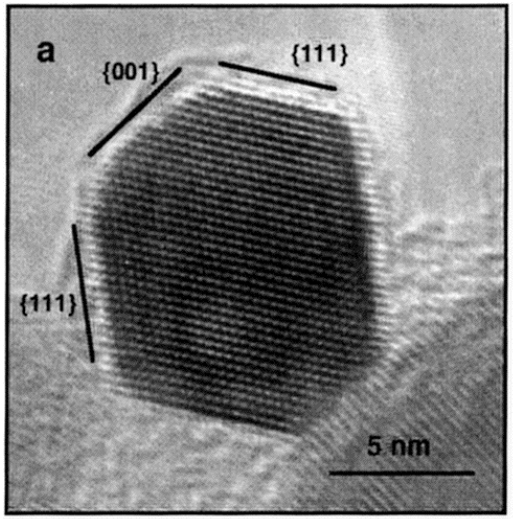

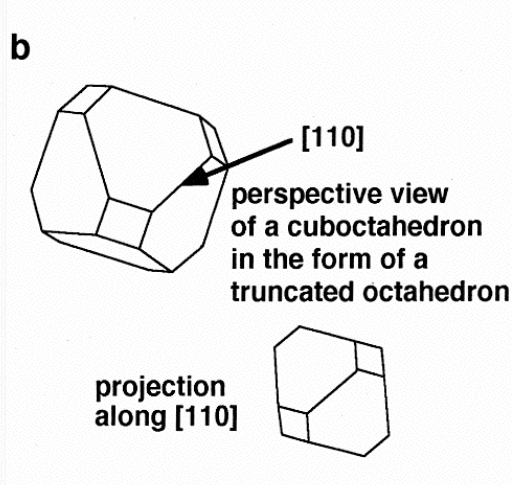

Cuboctahedral shape and its expected [110] projection.

Phase image

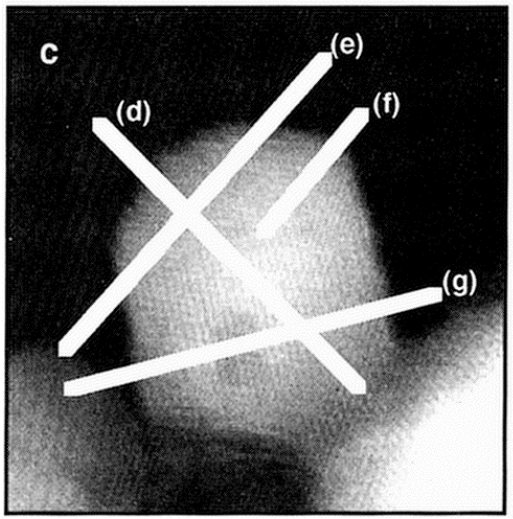

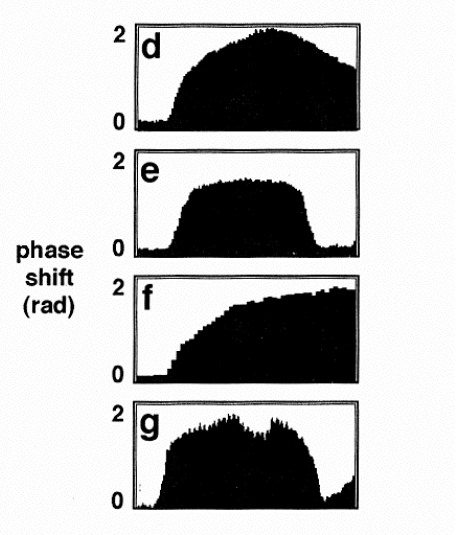

Line profiles across the phase image. A void in the particle is seen in the bottom profile.

Allard, L.F., E. Voelkl, A. Carim, A.K. Datye, and R. Ruoff
Nanostructured Mater. 7, 137 (1996)

The mean inner potential - dynamical effects

Mean inner potential contribution to phase shift

Dynamical simulations of spatially averaged phase shift for Pt as a function of specimen thickness

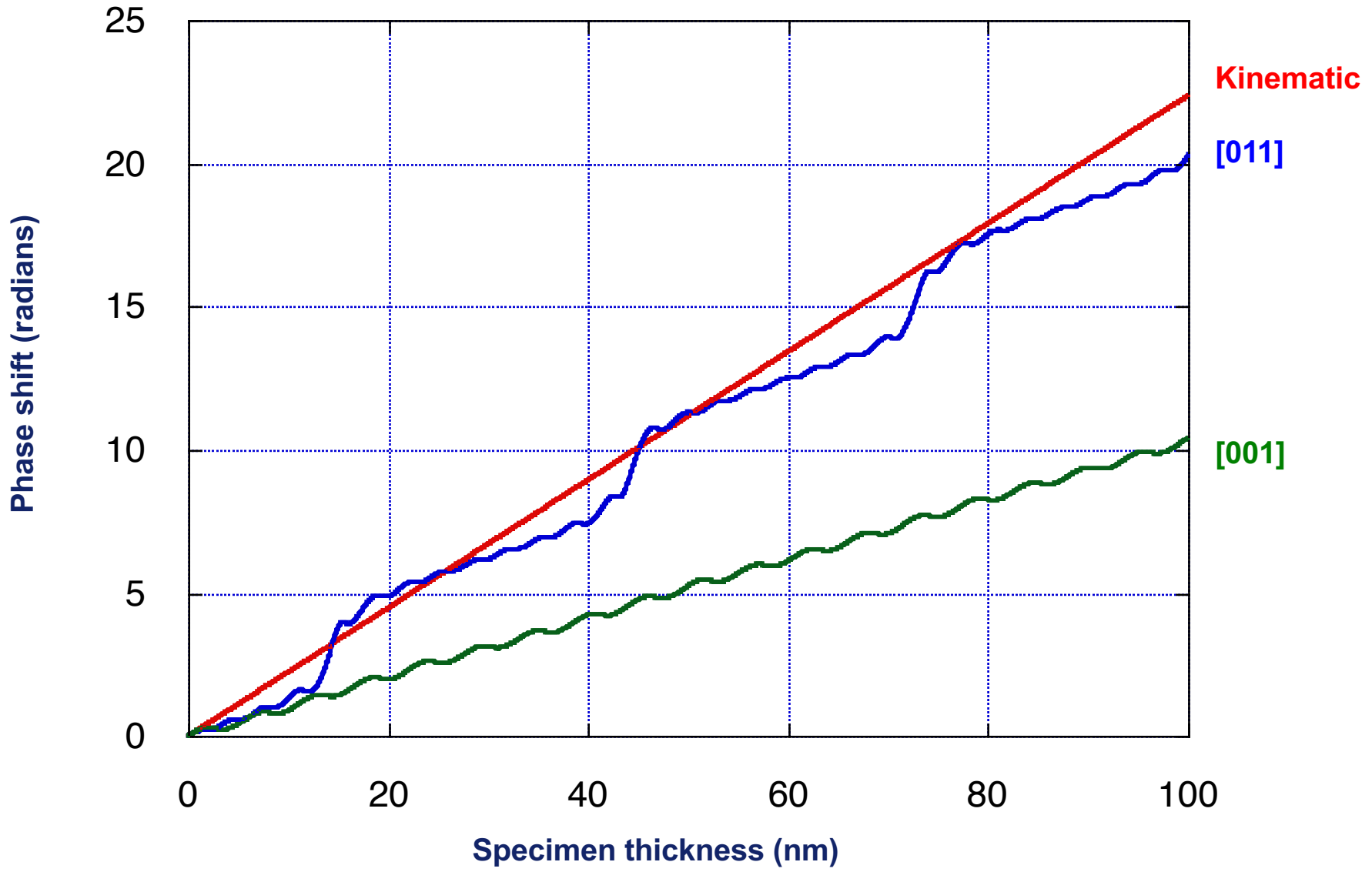

The mean inner potential - surface effects

Mean inner potential contribution to phase shift

Acta Cryst. (1994). A50, 33–45

On the Average Coulomb Potential (Φ_0) and Constraints on the Electron Density in Crystals

BY M. O'KEEFFE

Department of Chemistry, Arizona State University, Tempe, AZ 85287, USA

AND J. C. H. SPENCE

Department of Physics and Astronomy, Arizona State University, Tempe, AZ 85287, USA

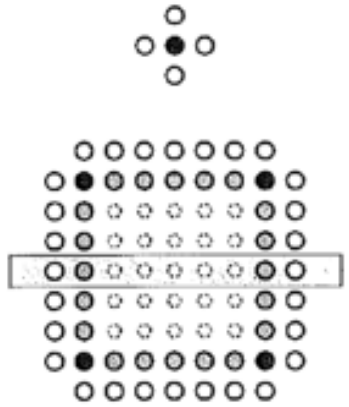

Fig. 5. Top: A layer of an octahedral charge distribution. Filled circle = $6q$, open circles = $-q$. Bottom: A layer of a crystallite made by repeating the octahedral charge distribution. Open circles = $-q$, lightly shaded circles = $+q$, heavier shaded circles = $+2q$.

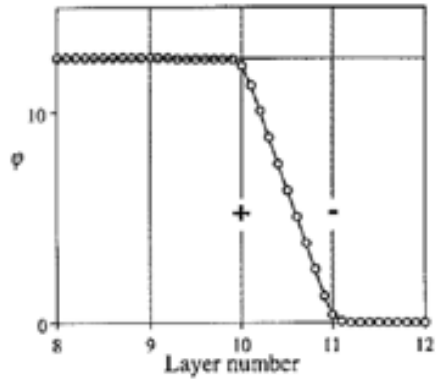

Fig. 6. The potential (in units of q/a), averaged over a square of side a, normal to the face of a crystallite such as that in Fig. 5. The crystallite is made from $21 \times 21 \times 21$ units of an octahedral basis of Gaussian charges with $\eta = 0.2a$. The dipole layer is between layers 10 and 11. The dotted line corresponds to $\varphi = 4\pi q/a$.

However, we call attention to the possibility of substantial dipole layers occurring on the surfaces of crystals in certain circumstances. Thus, if there were a monolayer of atoms of very different electronegativity adsorbed on all the surface of a crystallite at low temperatures, the surface dipole moment could easily be very much larger than that estimated above and easily measurable effects should be found.

With recent developments in electron holography (Tonomura, 1987) and of methods for properly taking into account dynamical effects in electron diffraction (Spence & Zuo, 1992), it is anticipated that accurate values of Φ_0 will soon be available for a variety of materials. We note that possible effects of surface dipole layers must be carefully evaluated; indeed, in appropriate systems with deliberately adsorbed surface layers, measurements of Φ_0 could be used to determine the density and sign of surface dipoles.

Electron holography of dopant potentials in semiconductor devices

Off-axis electron holography of electrostatic potentials

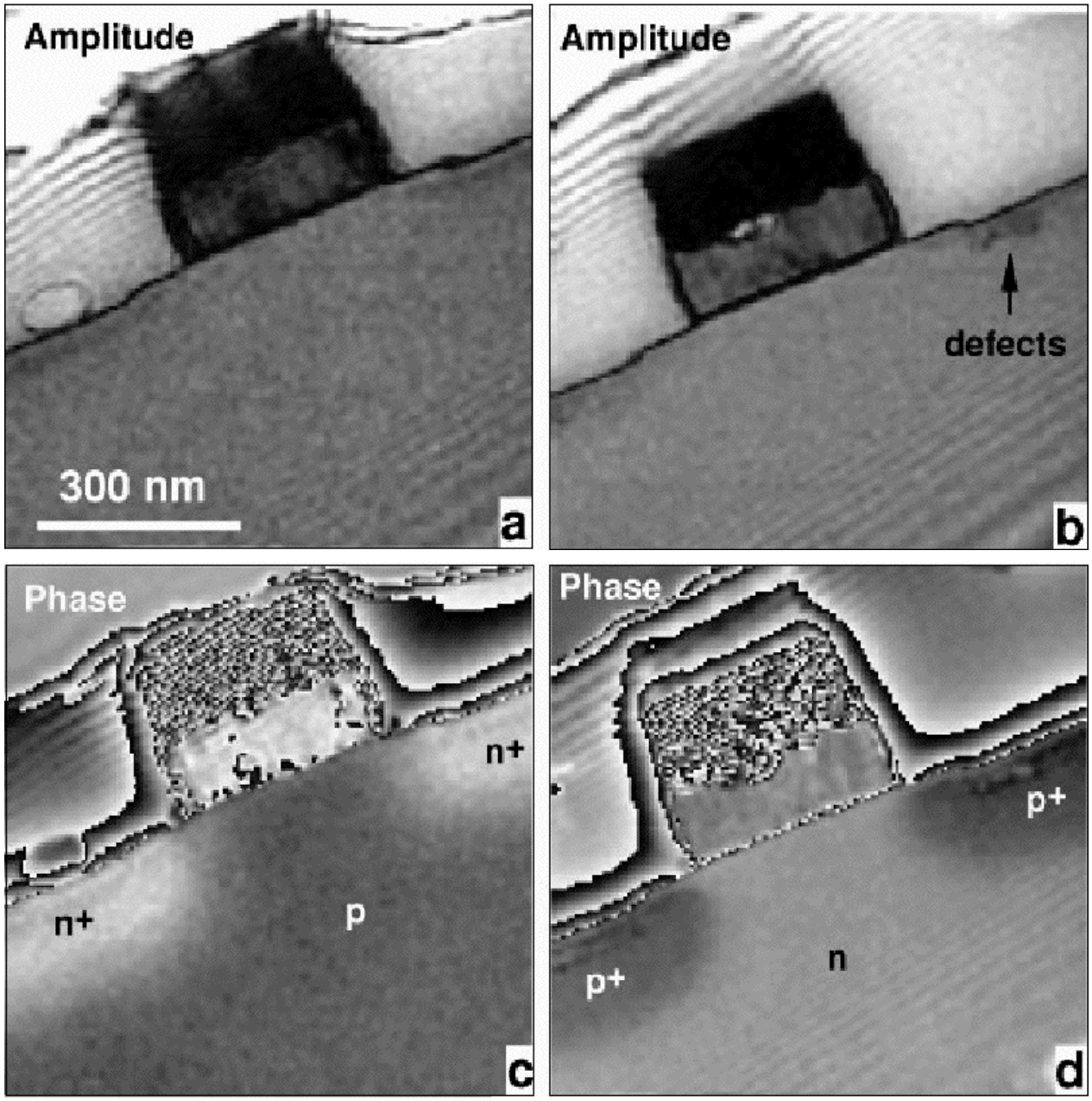

Amplitude images of 0.35 μm channel length *n*-MOS and *p*-MOS transistors

Phys. Rev. Lett. 82, 2614 (1999)

Corresponding phase images

Off-axis electron holography of electrostatic potentials

Electrostatic potentials in doped semiconductors

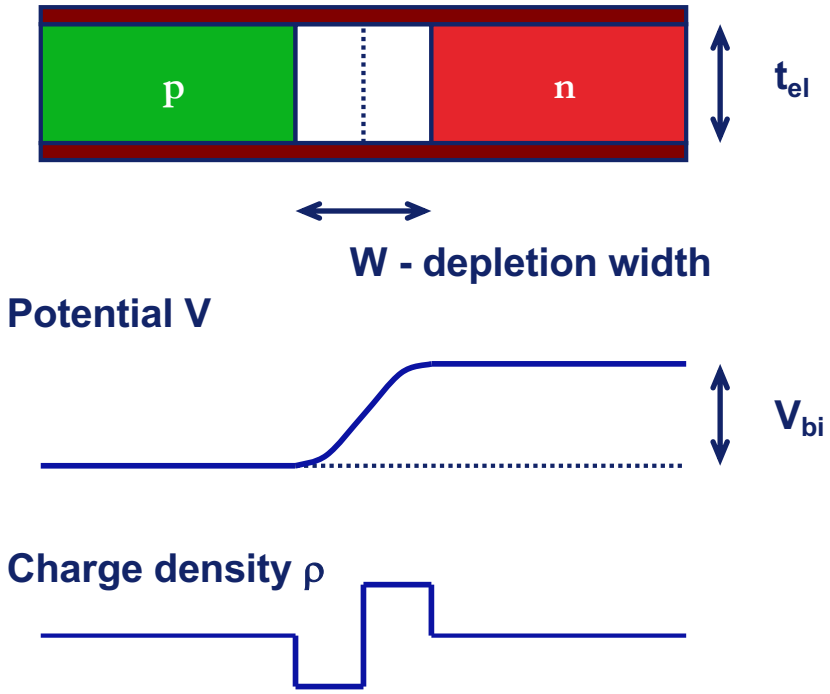

$$\Delta\phi = C_E(V_{bi}+V_{appl})t_{el}$$

Dopant potentials in semiconductors

Experimental phase profiles

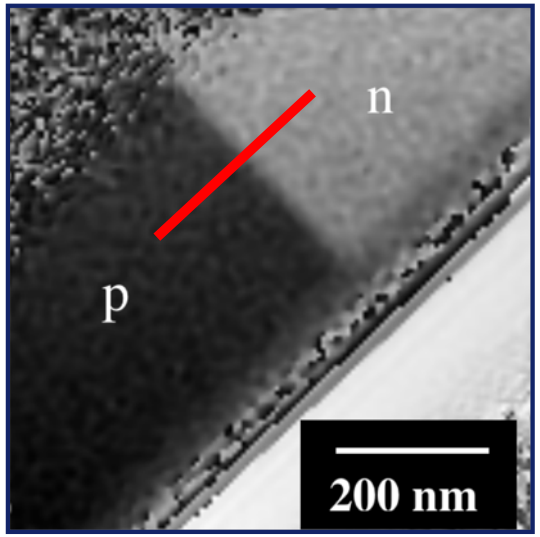

Unbiased

vs. sample thickness

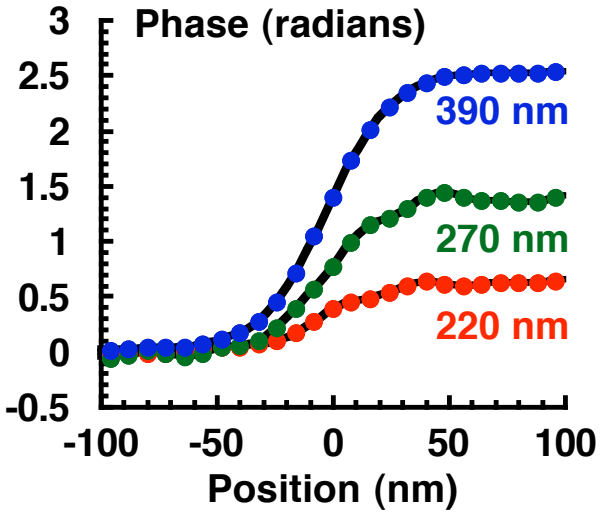

Different FIB sample for each crystalline thickness

Alison Twitchett-Harrison

Dopant potentials in semiconductors

Silicon

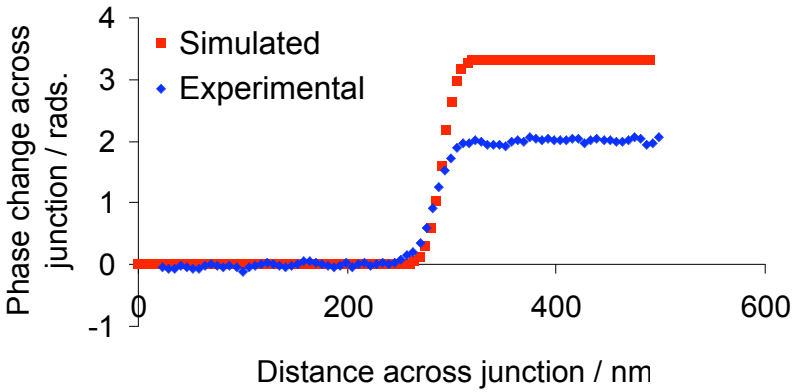

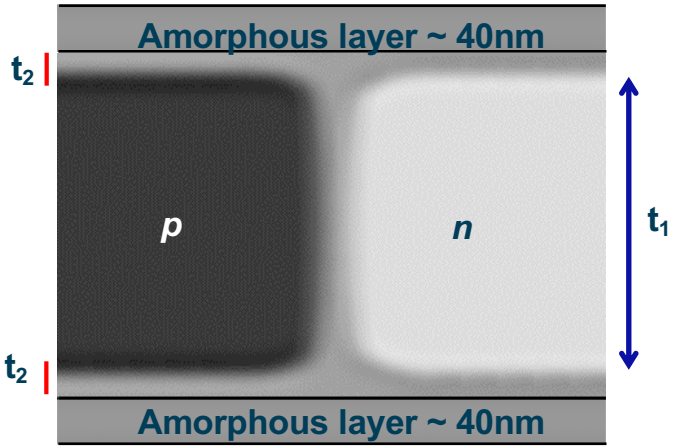

t_1 = 288nm and t_2 = 91nm

GaAs

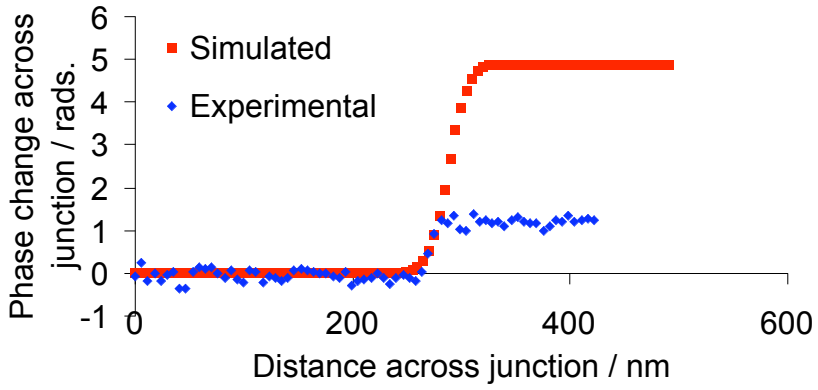

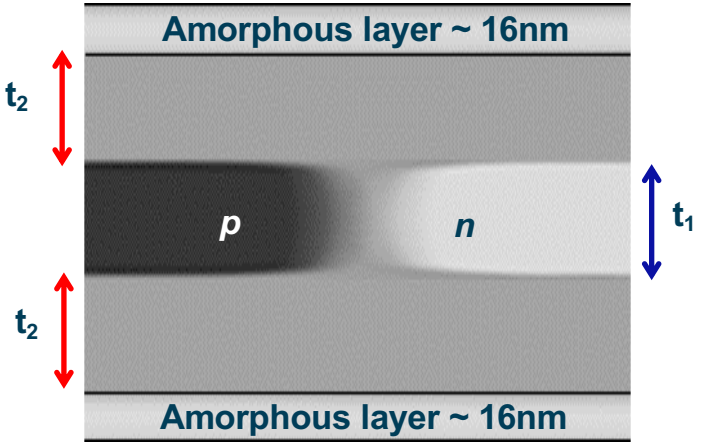

t_1 = 120nm and t_2 = 175nm

David Cooper
Alison Twitchett-Harrison

Electrostatic potential mapping in 3D

Electron holographic tomography of a Si p-n junction

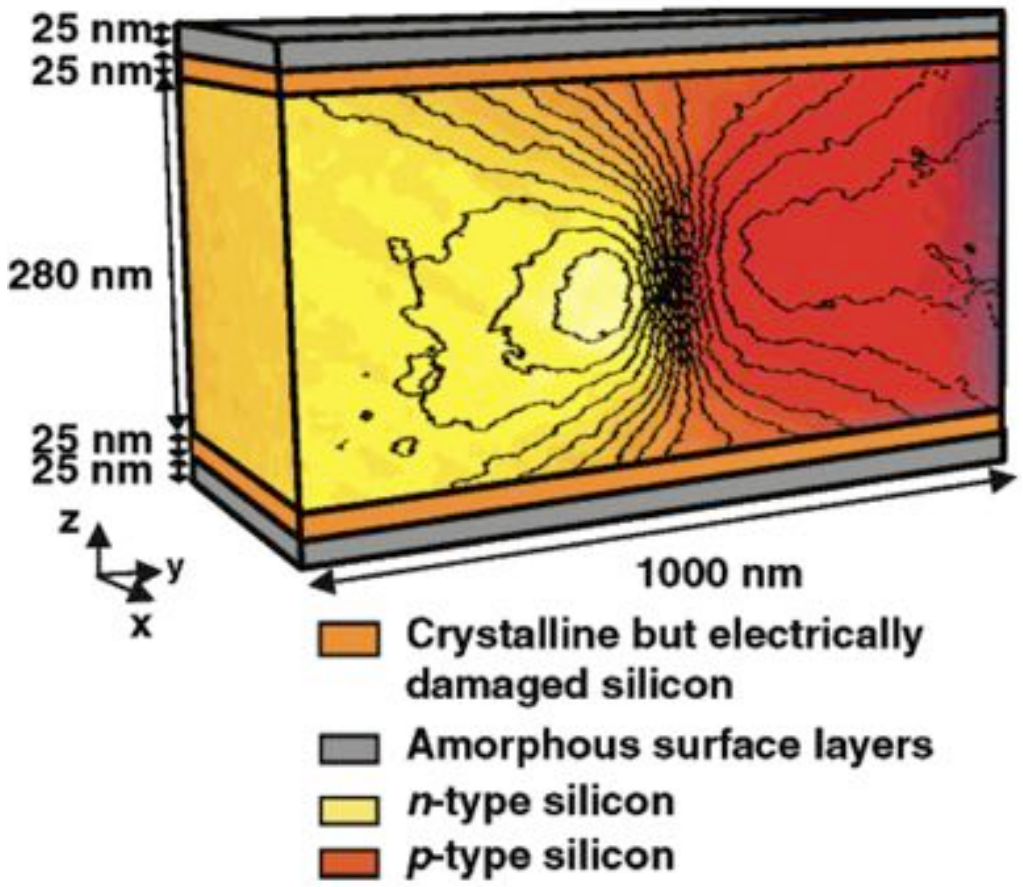

Alison Twitchett-Harrison
Tim Yates

Electrostatic potential mapping in nanowires

Electron holographic tomography of a core-shell nanowire

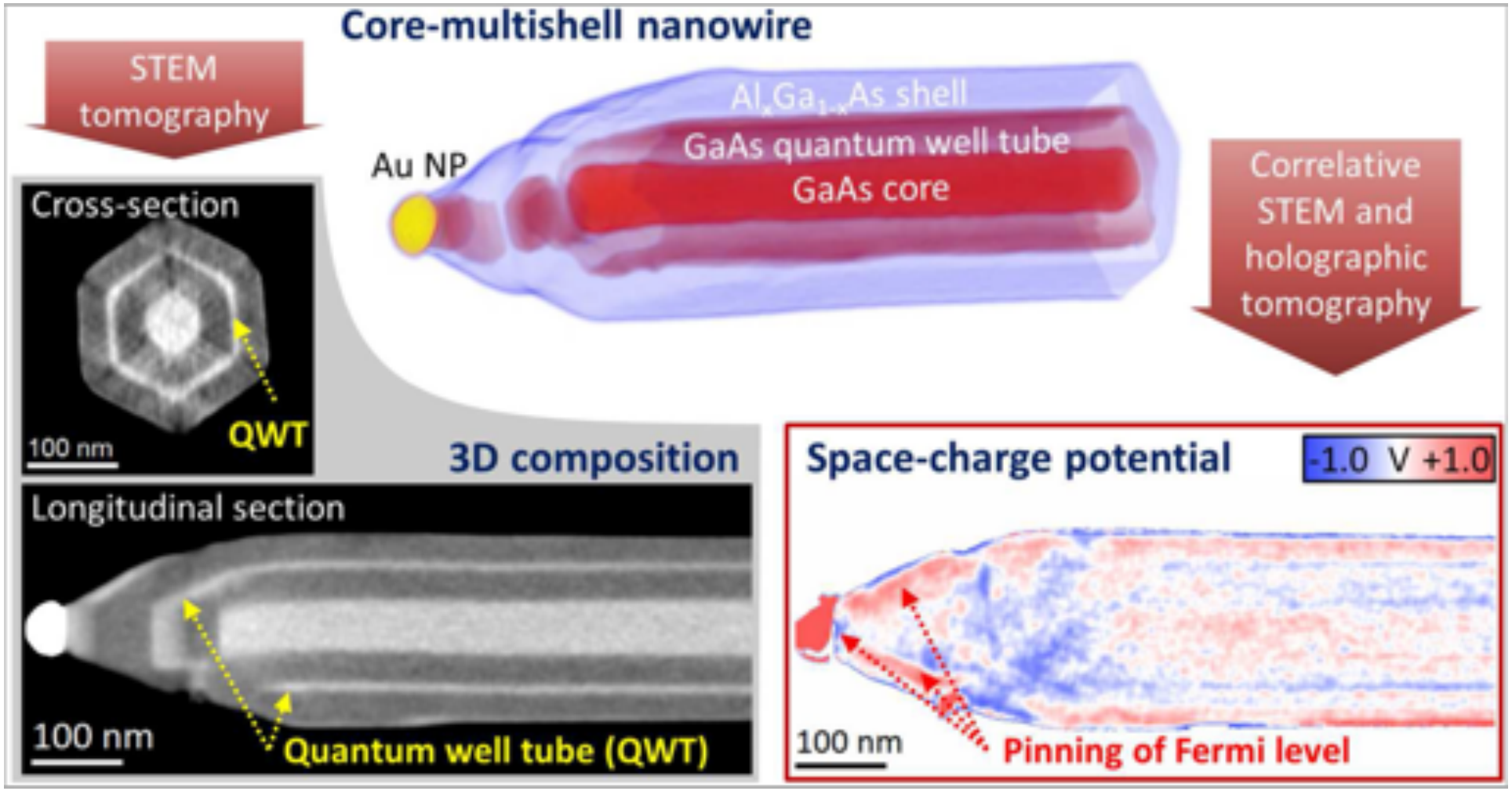

Three-dimensional composition and electric potential mapping of III–V core-multishell nanowires by correlative STEM and holographic tomography
D. Wolf et al. Nano Lett. 18 (2018), 4777-4784

Electrically contacted nanowires

Electron holography of Ge-Li_xGe core-shell nanowires during lithiation

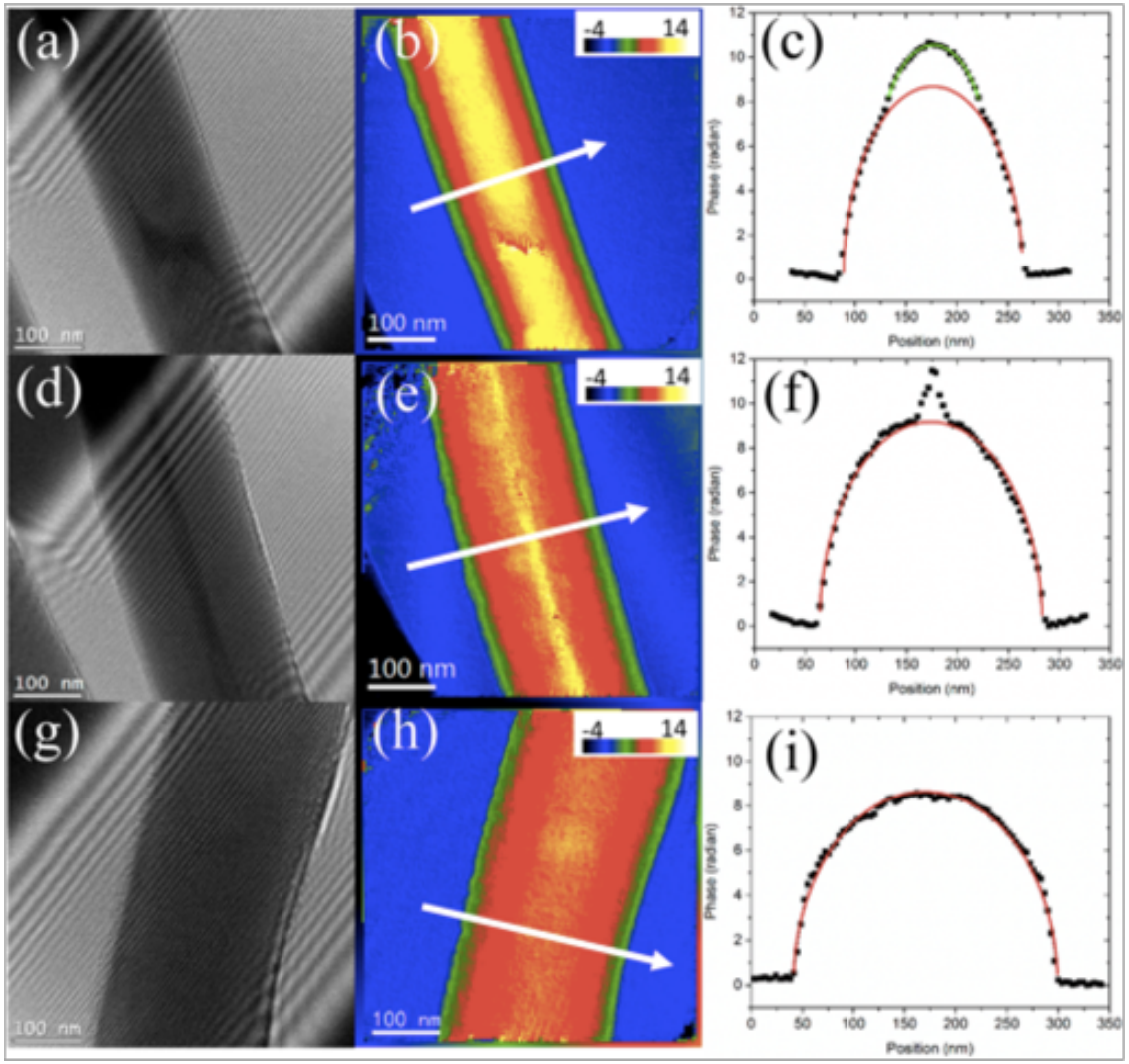

During *in situ* electrical biasing, lithiation leads to expansion of the Li_xGe shell and shrinking of the Ge NW core.

Electron holography shows that the surface of the core becomes negatively charged, while the inner surface of the shell develops a counterbalancing positive charge.

Direct mapping of charge distribution during lithiation of Ge nanowires using off-axis electron holography.
Z. Gan et al. Nano Lett. 16 (2016) 3748-3753.

High-resolution electron holography

Off-axis electron holography of electrostatic potentials

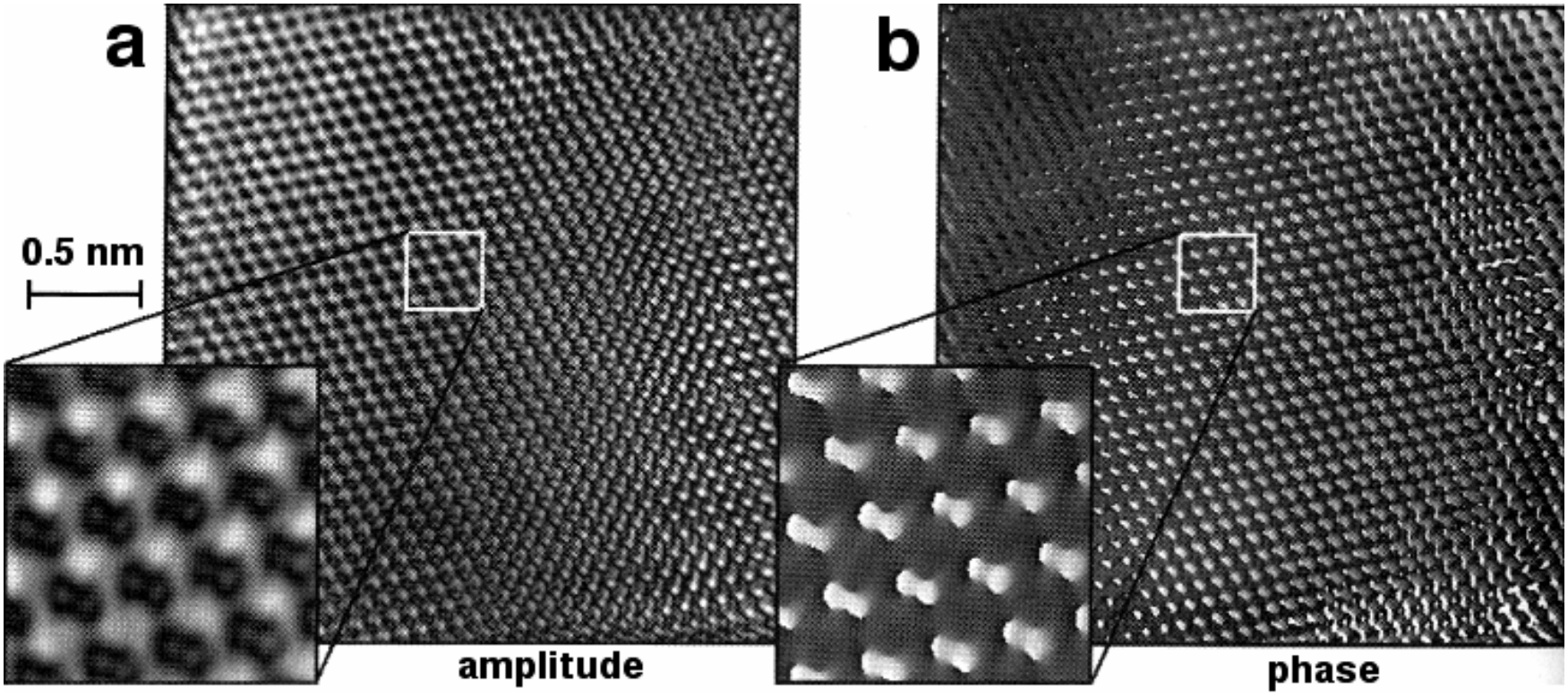

High-resolution (a) amplitude and (b) phase of the aberration-corrected object wave reconstructed from an electron hologram of [110] Si, obtained at 300 kV on a CM30 FEG-TEM. The spacing of the original hologram fringes was 0.05 nm. The sideband contained {111}, {220}, {113} and {004} reflections, corresponding to lateral information of 0.136 nm. The Si dumbbell structure is visible only after aberration correction.

A. Orchowski et al., *Phys. Rev. Lett.* 74, 399 (1995)

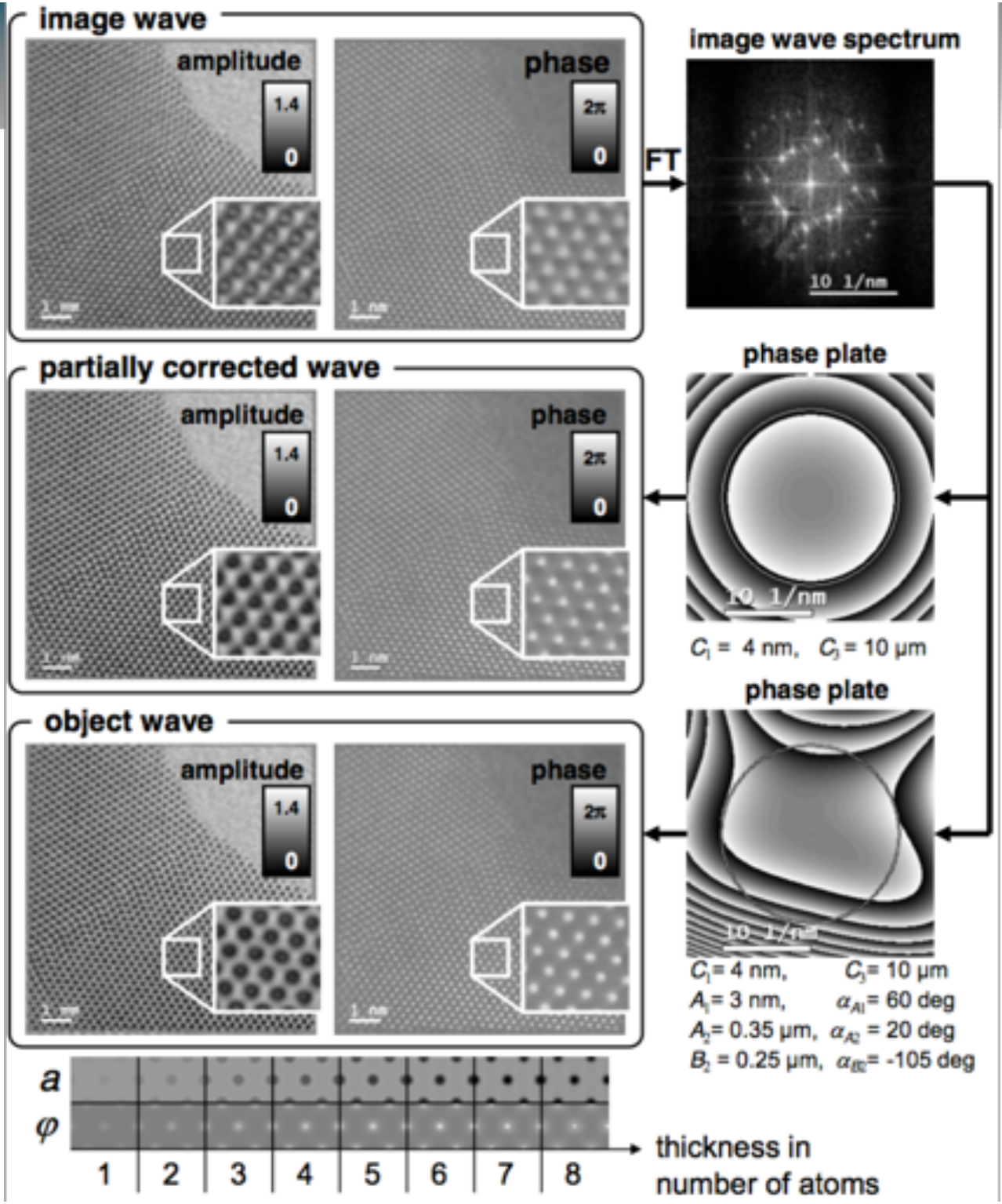

Martin Linck, Hannes Lichte

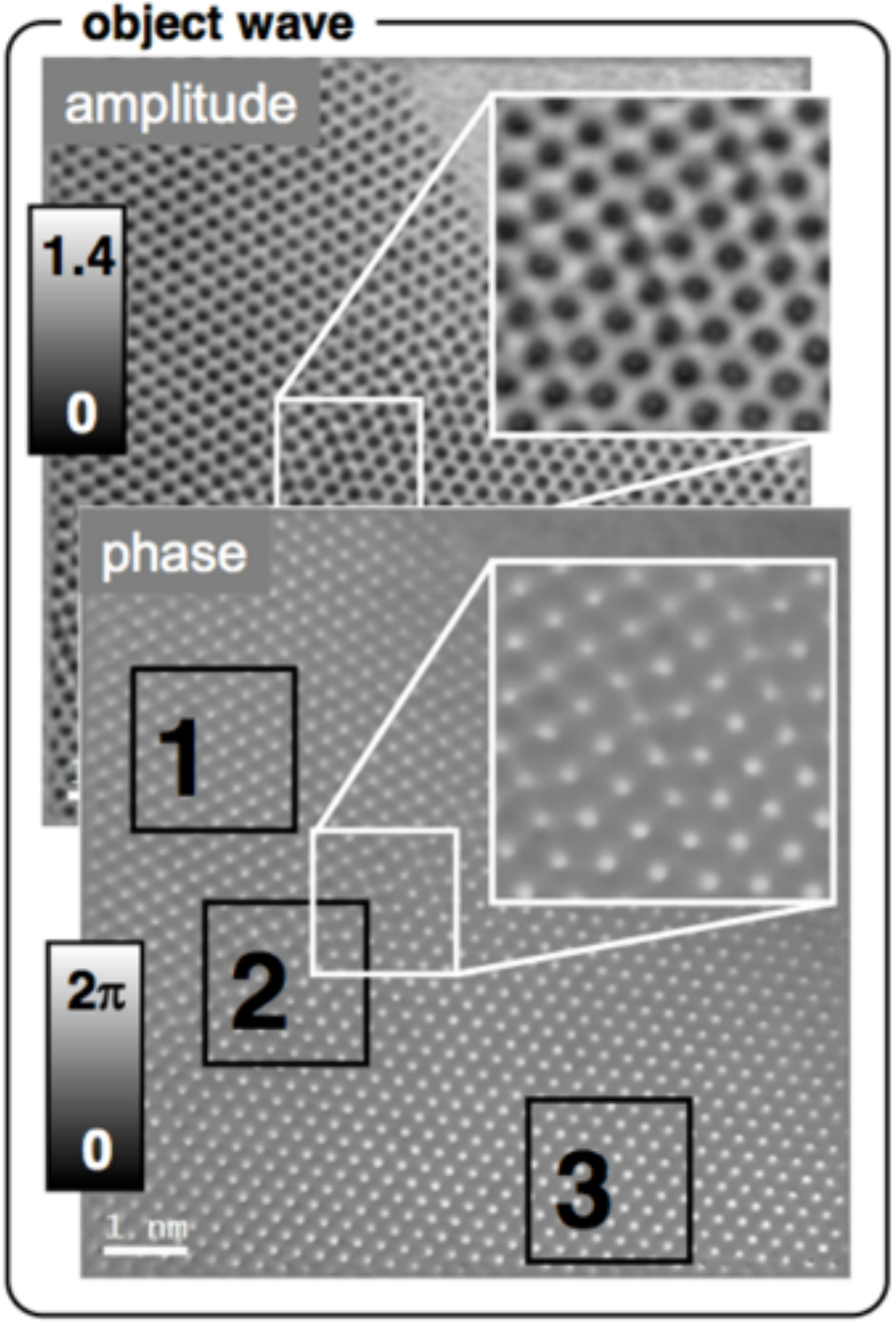

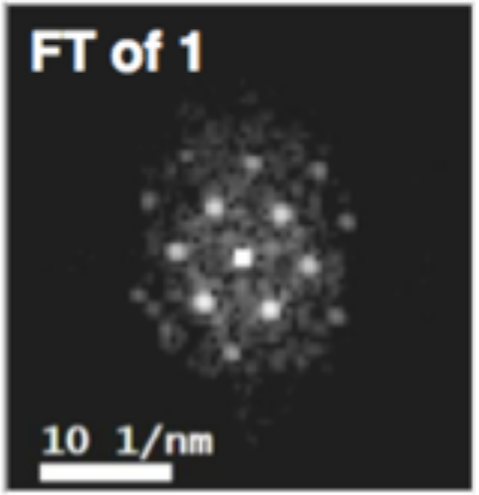

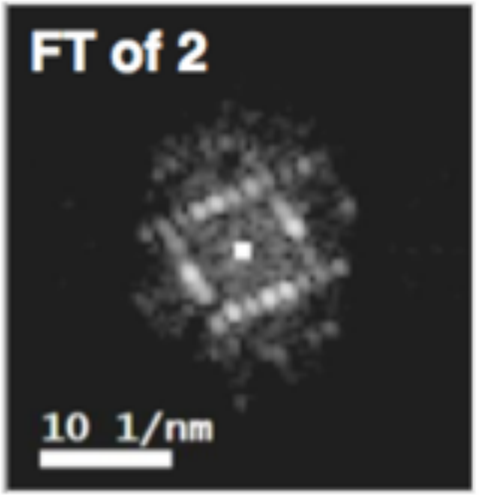

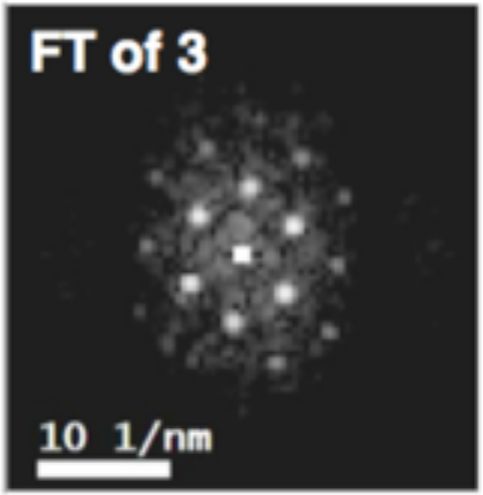

Martin Linck, Hannes Lichte

Other forms of electron holography

Other forms of electron holography

Phase-shifting electron holography

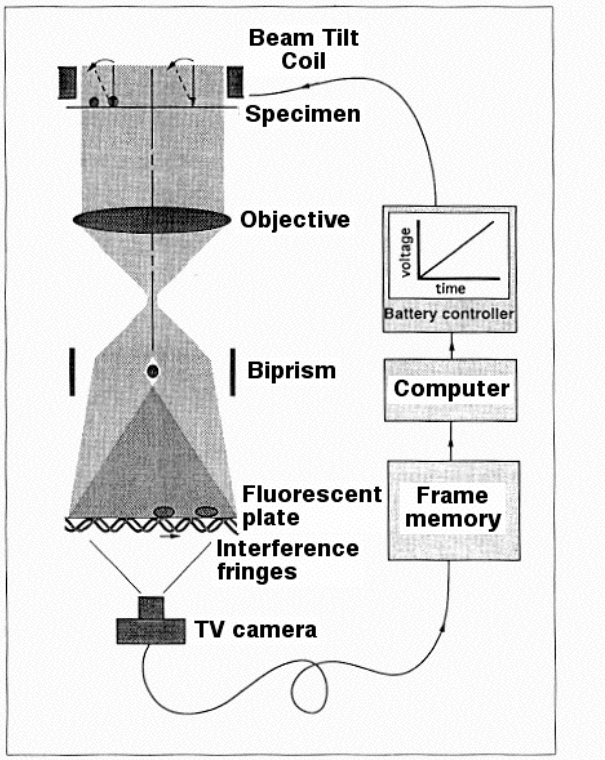

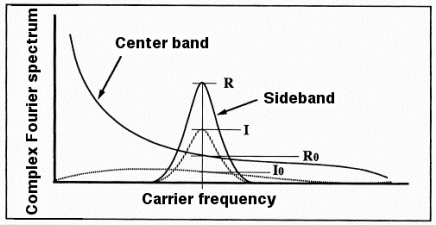

Schematic diagram of complex Fourier spectrum, with real and imaginary parts shown as solid and broken lines.

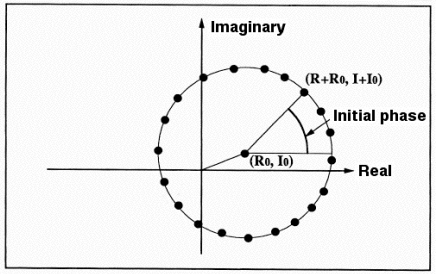

Complex plane, illustrating circular trajectory of spectrum data at carrier frequency.

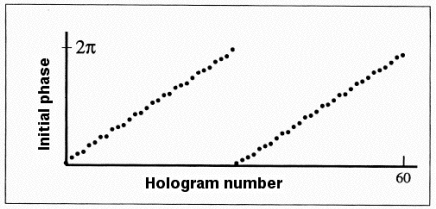

Initial phase data for series of holograms.

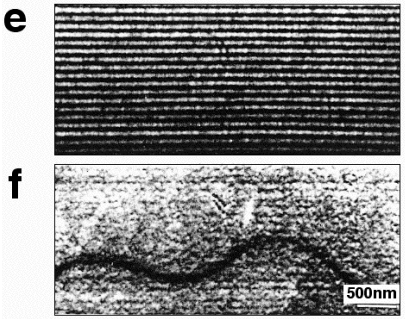

Hologram of flagellum filament and corresponding phase image, obtained from 96 holograms with initial phases of 0 to 4π. The maximum phase change due to the filament is 2π/40.

Ultramicroscopy 55, 209 (1994).

Acknowledgment: A. Tonomura

Other forms of electron holography

Hologram formation using a single-crystal film as an electron beam splitter

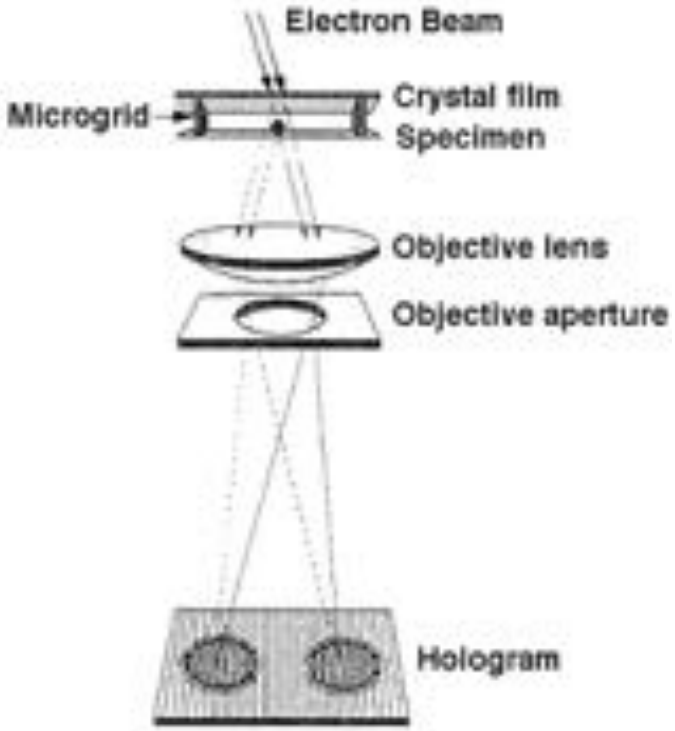

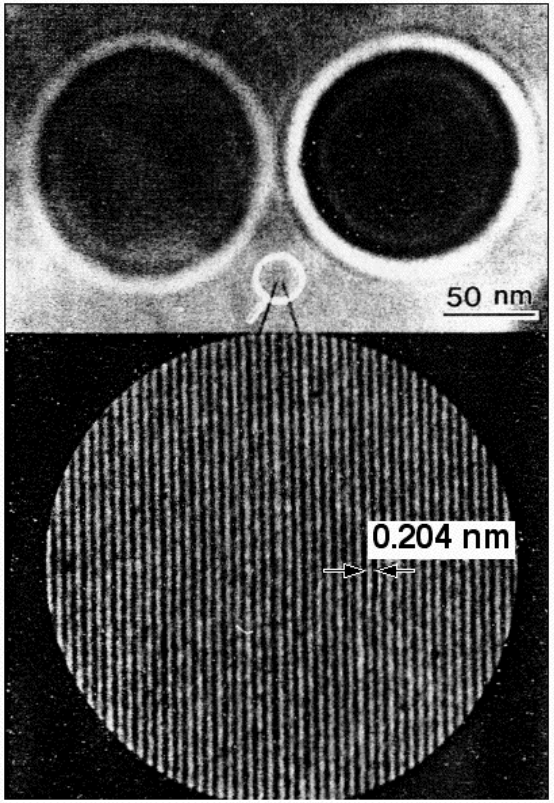

Fresnel hologram of a polystytrene latex particle containing approximately 1500 Au lattice fringes.

The left and right images are formed by the Bragg-reflected and direct beams, respectively.

Ultramicroscopy 53, 1 (1994).

Acknowledgment: A. Tonomura

Future directions

Future directions

- Working nanoelectronic and spintronic devices in the presence of multiple applied stimuli (currents, light, temperature, gas …)
- Improved temporal resolution: ultrafast and dynamic experiments
- Atomic resolution imaging of spins and charges
- Weakly scattering (biological and soft) materials

- Electron beam shaping …
- Hardware phase plates …

Limitations

- **Microscope & specimen:** **cleanliness and stability**
- **Image acquisition:** **automation of workflows**
- **Unwanted effects:** **electron beam induced charging and damage**

Magnetic nanocrystals again

Off-axis electron hologram of magnetic nanocrystals

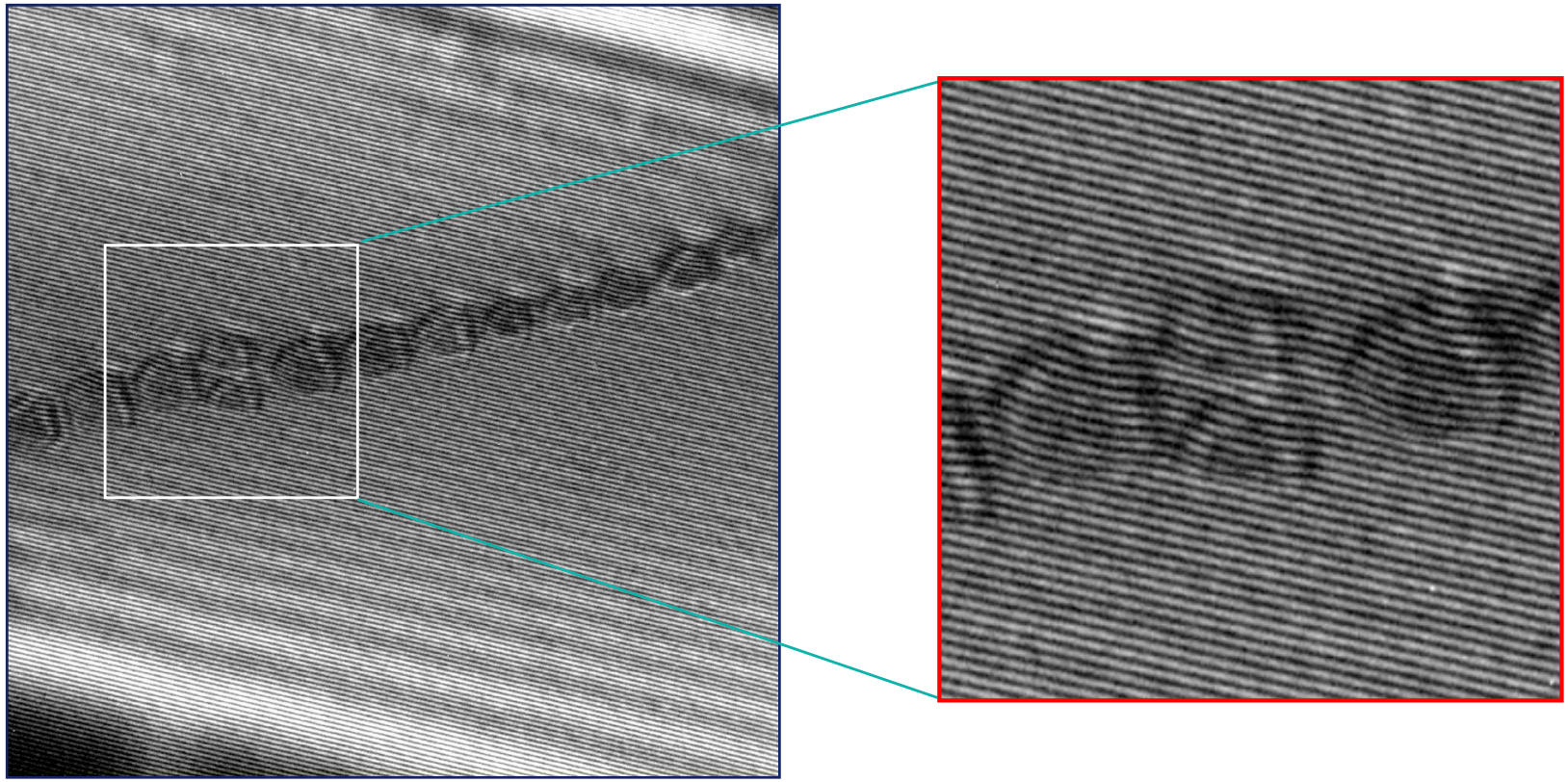

Electron hologram acquired in magnetic-field-free conditions
3.9 nm interference fringe spacing

Electron holography of magnetite crystals in magnetotactic bacteria

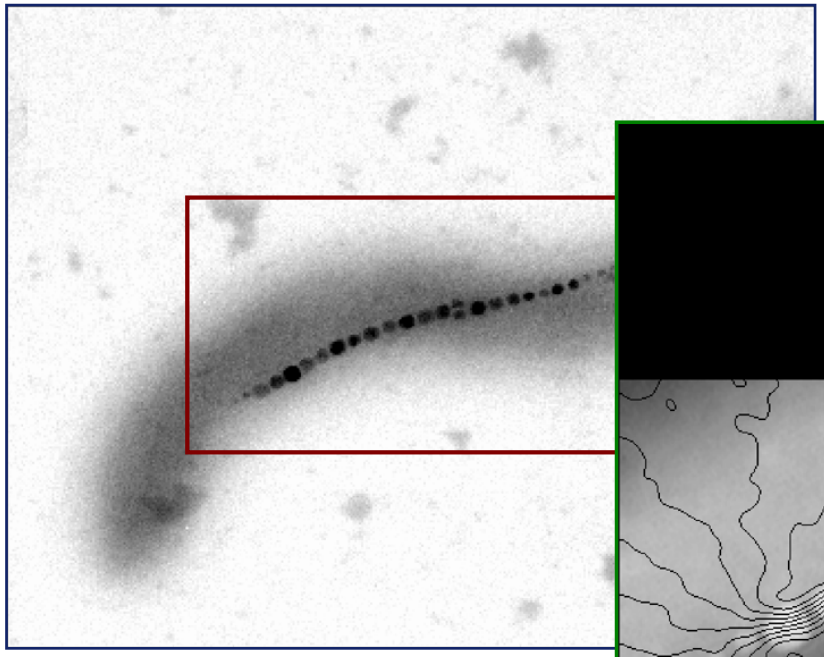

Magnetospirillum magnetotacticum strain MS-1

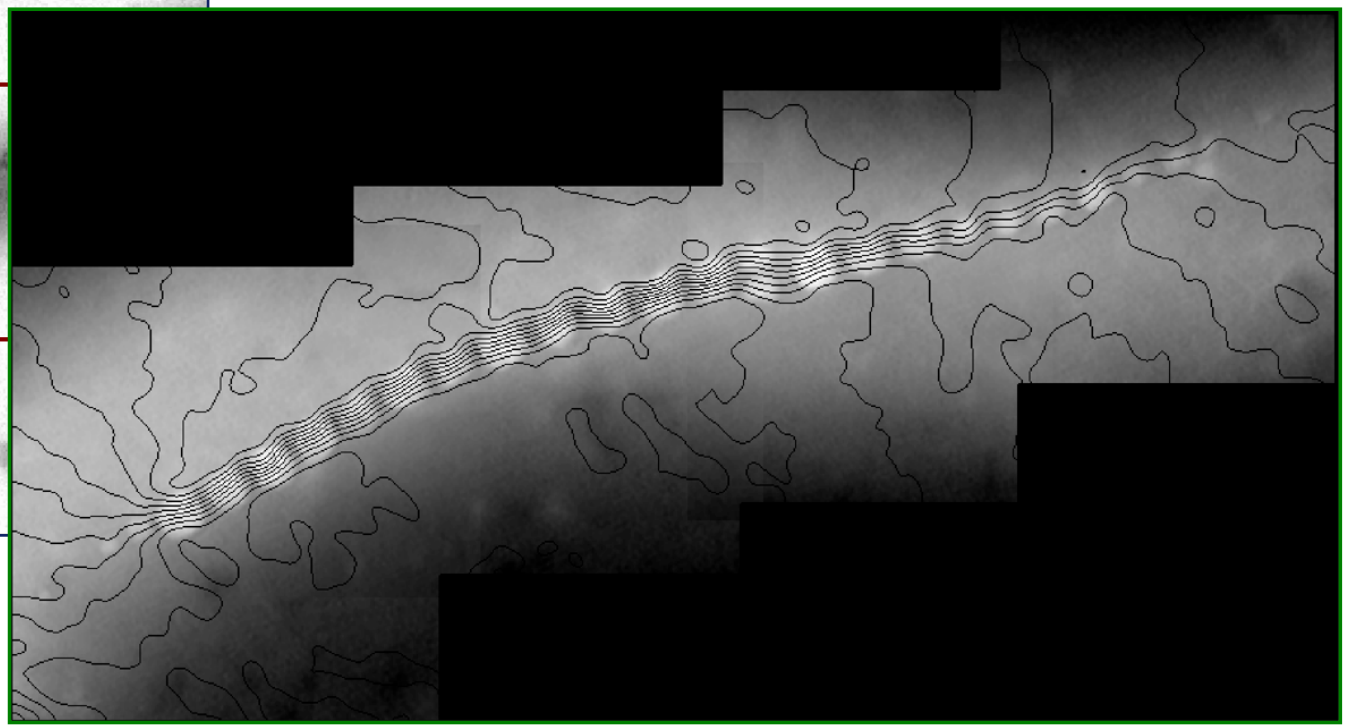

1200 nm long chain.
Twenty-two 45 nm crystals separated by 9.5 nm.
Crystals are combinations of octahedron and cube forms.
<111> magnetic easy axis primarily parallel to chain axis.

0.064 radian contours formed from magnetic contribution to phase and overlaid onto mean inner potential contribution to phase.